

Department of Physics and Astronomy  
Heidelberg University

Fast, High Precision Low Noise Bipolar Power Supply for  
Magnetic Field Coils in Ultra-Cold Dysprosium Experiment

Bachelor Thesis in Physics  
submitted by  
**Lennart Hoenen**  
on the 16.04.2022

Supervisor and first examiner: Prof. Dr. Lauriane Chomaz  
Second examiner: Prof. Dr. Selim Jochim

## **Abstract**

In this bachelor thesis a high precision, ultra-low noise, bipolar, current source for the driving of magnetic coils is presented and the design of a set of rectangular coils to generate homogeneous fields inside a vacuum chamber is described. The field equations necessary to simulate the magnetic field of rectangular coils are explained and design choices to achieve a high field homogeneity are discussed. The theory of noise analysis by the use of a discrete Fourier transform and the theory of operational amplifiers is explained, to enable the description and analysis of a prototype of the power supply that will be used to power the magnetic field coils of a new ultra-cold dysprosium experiment. The prototype is tested on a set of coils and their time response is analyzed to test the capabilities of the PI-controller, that is part of the power supply.

## **Zusammenfassung**

In dieser Bachelorarbeit wird eine hoch präzise, rauscharme, bipolare Stromquelle für den Betrieb von Magnetspulen präsentiert und das Design eines rechteckigen Spulenkäfigs zur Erzeugung homogener Magnetfelder in einer Vakuumkammer wird beschrieben. Die zur Simulation von rechteckigen Spulen benötigten Feldgleichungen werden erklärt und der Entwurf von rechteckigen Spulenpaaren im Hinblick auf hohe Feldhomogenität wird erläutert. Der benötigte theoretische Hintergrund um Signalrauschen mit Hilfe einer diskreten Fourier Transformation durchzuführen wird geschaffen. Die Funktionsweise von Operationsverstärken wird erklärt um die Beschreibung und Analyse eines Prototypen der Stromquelle, welche in einem neuen ultrakalten Dysprosium Experiment verwendet werden wird, zu ermöglichen. Der Prototyp wird an einem Spulenpaar getestet und ihr Frequenz- und Zeitverhalten wird analysiert um das Leistungsvermögen eines PI-Regles, welcher Teil der Stromquelle ist, zu testen.

# Contents

<b>1</b>	<b>Introduction</b>	<b>1</b>
<b>2</b>	<b>Magnetic Coils in a Dysprosium Experiment</b>	<b>3</b>
2.1	Dipolar Interactions . . . . .	3
2.2	Feshbach Resonances . . . . .	4
2.3	Coil Design . . . . .	6
2.3.1	Design of Rectangular Coils . . . . .	7
2.3.2	Design of Intermediate Coils . . . . .	11
2.4	Eddy Currents . . . . .	12
2.5	Resulting Constraints on Power Supply . . . . .	13
<b>3</b>	<b>Noise Analysis</b>	<b>15</b>
3.1	Power Quantities and Root-Power Quantities . . . . .	15
3.2	Fourier Transformation . . . . .	16
3.2.1	Nyquist-Shannon Theorem and Aliasing . . . . .	17
3.2.2	Window Functions . . . . .	17
3.2.3	Scalloping Loss . . . . .	18
3.2.4	Normalisation of Fast Fourier Transform . . . . .	18
3.3	Noise Spectral Density . . . . .	20
3.4	Root Mean Square and Peak-Peak Noise . . . . .	21
<b>4</b>	<b>Design of Power Supply</b>	<b>23</b>
4.1	Overview . . . . .	23
4.2	Operational Amplifiers . . . . .	24
4.3	Active Current Control . . . . .	27
4.3.1	Current Measurement . . . . .	27
4.3.2	PI-Control . . . . .	29
4.3.3	Current Source . . . . .	31

<b>5</b>	<b>Experimental Results</b>	<b>35</b>
5.1	Optimisation of PI Parameters . . . . .	35
5.2	Current Sensing . . . . .	37
5.3	Risetime and Falltime . . . . .	38
5.4	Frequency Response . . . . .	41
5.5	Noise of Power Supply . . . . .	44
<b>6</b>	<b>Summary and Outlook</b>	<b>49</b>
<b>7</b>	<b>Bibliography</b>	<b>51</b>

# 1 Introduction

Ultra-cold quantum gas experiments, are an intriguing field of study as they allow the observation of novel quantum phenomena with a high degree of tunability and flexibility. Since the first creation of Bose Einstein condensates of rubidium and sodium in 1995 [1], atomic species, fermions and bosons alike, have been cooled down to the degenerate regime.

In a new ultra-cold quantum gas experiment being built under the supervision of Prof. L. Chomaz, dysprosium atoms are to be cooled and trapped to investigate their behaviour as a quantum fluid. The element dysprosium is especially interesting, as it is the element with the highest magnet moment and thus exhibits a strong dipolar properties. Therefore in a dysprosium gas atoms not only exhibit short range contact interactions but also long range dipolar interactions. In particular, by tuning the interaction strength of the contact interactions using Feshbach resonances, one is able to tune the relative strength between the two aforementioned interactions. In this new experiment, the dysprosium atoms will be trapped in a combination of optical and magnetic potentials in order to explore the intriguing behaviour of two dimensional quantum gases. As magnetic fields are used extensively for the manipulation of quantum gases and play an important role in most quantum gas experiments, electromagnetic coils have to be carefully designed to create the needed magnetic fields. For the new experiment, magnetic coils will be used to create offset fields in arbitrary directions and a quadrupole field gradient around the centre of the main vacuum chamber. Not only do the coils need to be designed and manufactured precisely, but to allow for accurate tuning and highly flexible manipulation of the quantum gas, an equally precise current source has to be built to supply the coils.

The design of two pairs of the required offset coils will be described in the first part of this bachelor thesis. Then the design of a ultra-low noise power supply capable of fast and accurate driving of magnetic coils is presented and a prototype of the same is characterised.



# 2 Magnetic Coils in a Dysprosium Experiment

## 2.1 Dipolar Interactions

Dysprosium is an especially interesting element to study, as it has a very high magnetic moment. Not only are different optical transitions accessible for efficient trapping and cooling, but in its ground state it has a rather special electron configuration [2]:

$$[Xe]4f^{10}6s^2$$

where  $[Xe]$  represents the full electron configuration of the noble gas xenon. This means that while the outermost  $6s$  shell is completely filled, four electrons in the  $4f$  shell are unpaired and according to Hund's rules, the states with orbital angular momentum projection quantum numbers  $m_l = \{3, 2, 1, 0\}$  in the  $f$  shell are unoccupied completely. This gives rise to a total orbital angular momentum of  $L = 0\hbar + 1\hbar + 2\hbar + 3\hbar = 6\hbar$ . The spin angular momentum of the 4 unpaired electrons is  $S = 4 \times \hbar/2 = 2\hbar$ . Therefore, the total angular momentum, which couples as  $J = L + S$  is  $J = 8$ . The magnetic moment  $\mu_m$  can be calculated as [3]:

$$\mu_m = - \sum_{m_l=0}^3 g_l m_l \mu_B - \sum_{i=0}^3 g_s \frac{\mu_B}{2} \approx -10\mu_B \quad (2.1)$$

where  $g$ -factors are  $g_l = 1$  and  $g_s \approx 2$  and  $\mu_B$  is the Bohr magneton.

As a result of this high magnetic moment, the dipole-dipole interaction between dysprosium atoms is up to 100 times stronger than in alkali elements. The magnetic dipole-dipole interaction potential of two dysprosium atoms within an external magnetic field can be described as [4]:

$$V_{dd} = \frac{m\mu_0\mu^2}{4\pi} \frac{1 - 3\cos(\theta)^2}{r^3} \quad (2.2)$$

where  $\theta$  is the angle between the external field and the vector connecting the two atoms. Thus, the interaction potential between the atoms depends strongly on their relative position. If they lie 'head-to-tail' oriented along the external magnetic field,  $\theta$  equals zero,  $\cos(\theta) = 1$  and the potential is negative: the magnetic dipoles attract each other. If they lie 'side-by-side' the angle will be  $\theta = 90^\circ$  and the potential is positive and they repel each other. In other words: the interaction potential is anisotropic.

The notion of a 'long-range' interaction, for a potential scaling with  $r^{-3}$  is justified by comparing it to other interactions. For non-dipolar atoms in the low temperature regime, the contact interaction can be modelled by a short range potential [3]:

$$V(r) = g\delta(r) = \frac{4\pi\hbar^2}{m}a \cdot \delta(r) \quad (2.3)$$

where  $\delta(r)$  is the delta function,  $m$  is the mass of a single collision partner and  $a$  is the  $s$ -wave scattering length.  $s$ -wave scattering refers to the scattering of a spherically symmetric wavefunction of quantum number  $s$ , and is the dominant process at low temperatures for short range interactions. As this pseudopotential, given by a delta function and only dependent on a scattering length  $a$ , is sufficient to describe the interactions in a cold quantum gas, it is clear that the contact interaction is really 'close-range' and a dipolar interaction scaling with  $r^{-3}$  can be called 'long-range'.

To be able to study the effect of dipolar interactions in a dysprosium quantum fluid, one can make use of the phenomenon of Feshbach resonances. These resonances allow to tune the contact interaction and thus to tune the relative strength between short range (contact) and long range (dipolar) interactions, by applying a magnetic field. This will be explained shortly in the coming section.

## 2.2 Feshbach Resonances

Depending on the internal structure of the collisions partners, there may exist multiple interaction potentials. These can couple together such that the scattering properties are strongly modified [2]. To explain the basics of Feshbach resonances, let us consider two coupled potentials as depicted in Fig. 2.1a). The background potential  $U_{bg}(r)$  connects asymptotically to the energy of two free atoms in an ultra-cold gas. Another potential  $U_c(r)$  is energetically higher than the free energy of the atoms at large distances and is therefore not available for the atomic interaction. It is thus called the *closed channel*, while the other potential, as it is the only energetically potential, is called the *open channel* for the collision process. These different channels correspond to different sets of quantum

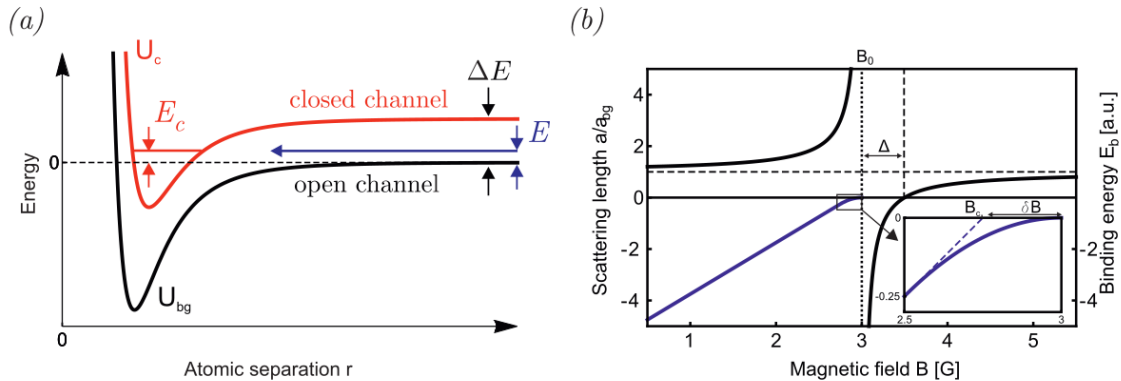


Figure 2.1: **Illustration of Feshbach resonances** as taken from [2] a) Schematic of the open and closed interaction channel. b) Relative scattering length  $a/a_{bg}$  (black) and molecular binding energy  $E_b$  (blue) as a function of external magnetic field  $B$ .

numbers and might therefore differ in the orbital angular momentum projection quantum number  $m_l$ .

The closed channel has to support at least one bound state with an energy  $E_c$  near the asymptotic value of the open channel. If the small energy  $E$  of the ultra-cold collision partners matches the energy  $E_c$ , the coupling between the two channels is magnified and a strong mixing of the two channels occurs. This can lead to the temporary formation of a weakly bound molecule of the two collision partners. The result is a divergence of the scattering length  $a$  of the interaction.

The energy of the two channels is proportional to the product of the external magnetic field and their magnetic quantum number  $m_l$ . If the two channels have a difference in  $m_l$ , their energies and their energy difference  $\Delta E$  is dependent on an external magnetic field, due to the Zeeman effect. Therefore, by applying a homogeneous magnetic field, the energy  $E_c$  can be tuned to match that of the interacting atoms and a Feshbach resonance can be induced.

The dependence of the  $s$ -wave scattering length  $a$  on the external magnetic field can be described by [5]:

$$a(B) = a_{bg} \left( 1 - \frac{\Delta}{B - B_0} \right) \quad (2.4)$$

where  $a_{bg}$  is the scattering length of the potential  $U_{bg}$ ,  $B_0$  is the field at which the resonance occurs,  $\Delta$  is the width of the resonance (in units of magnetic field strength) and  $B$  is the applied magnetic field. Thus the scattering length of the contact interactions can be tuned. This is shown in Fig. 2.1b). There the divergence of the scattering length  $a$  around  $B_0$  is

visible in black. The molecular binding energy of the scattering partners is drawn in blue and show a linear behaviour as the distance between the atoms is large. Due to coupling, the binding energy deviates from this linear behaviour around the resonance point.

For the case of dipolar atoms such as dysprosium, this is especially interesting as it allows tuning of the relative strength of the dipol-dipol interaction and contact interaction. In other words via the application of a magnetic field, one can manipulate the atoms to go from a regime where only contact interactions are relevant to one, where only dipolar interactions are relevant.

## 2.3 Coil Design

To be able to generate a magnetic field up to 15G in any direction and a 6G/cm gradient in z-direction (vertical and perpendicular to atomic path), three sets of coils were designed. The gradient is generated with two circular coils in Anti-Helmholtz configuration and 120 turns of 500  $\mu\text{m}$  FSP18 Solabond wire by Elektrisola<sup>1</sup>. It can be baked at 150 – 170°C to bond the wires together stably and improve the heat conductivity inside the coil. The field in z-direction is generated by a pair of circular coils with 60 turns of the same wire in Helmholtz configuration.

Both these pairs of coils are positioned inside a custom designed reentrant viewport, to be as close as possible to the dysprosium atoms and where designed by Joschka Schöner. They are wound around a water-cooled copper holder to further improve cooling of the coils.

To allow for an offset field in x and y direction (both horizontal directions) and to compensate stray magnetic fields such as the earth's magnetic field, a small cage of rectangular coils was designed around the main chamber by the myself. Its design will be discussed in further detail below.

Due to unforeseen delays, the custom viewport and therefore the two sets of cir-

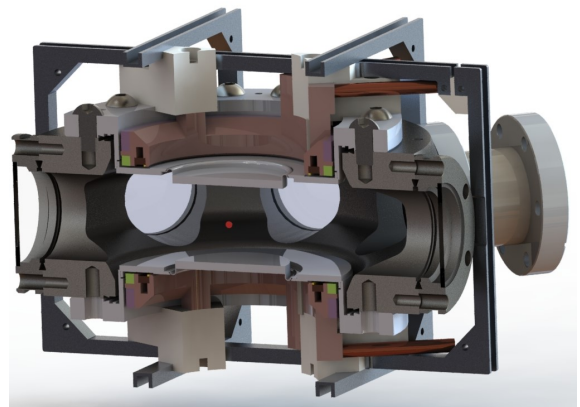


Figure 2.2: 3D model of main chamber with coils inside custom viewport and rectangular coil cage, and a red dot indicating the position of the atoms

<sup>1</sup><https://www.elektrisola.com/en/Products/Selfbonding-Wire/Types>

cular coils within can not be used immediately. To solve this problem, two intermediate coils were designed, to be used around a standard CF100 viewport. These will be used in the experimental analysis of the power supply below (sec. 5) and will be described shortly below.

### 2.3.1 Design of Rectangular Coils

The aim of the rectangular coil cage, which will be called xy-cage from now on, is to provide a homogeneous magnetic field offset in an arbitrary (horizontal) direction. The coils should provide a homogeneous field, that can be changed reasonable fast while they should not consume too much power. In general, the bigger the coils are, the greater the homogeneity will become, but the inductance and with it the time response of the coils will become larger. Also an increase in size will mean an increase of the power needed to create a certain field strength in the centre of the coils. Finally the size of the design will of course be limited by the constraints of the surrounding experimental setup. Most importantly, the main chamber rest only 40mm over an optical table that supports the optical setup. Thus, as the field homogeneity in the centre of the cage might improve with the cage size, having a big compensation cage around the main chamber of the experiment will result in slower switching times and may necessitate cutting the optical table and might cause obstruction of the optical path. Therefore, the design of a small cage around the chamber, that provides the desired fields was attempted. By simulating the field of rectangular coils in Helmholtz configuration, it was found that a set of two interlocking pairs of rectangular coils can provide the required field, while fitting around the main chamber and without taking up unnecessary space. To be able to simulate the magnetic field of a rectangular coil, the field was calculated according to a derivation by M. Misakian [6]. For a perfectly rectangular wire which is centred with the coordinate system and lies in the x-y-plane, Misakian gives the following equation to calculate the vector components  $B_x$ ,  $B_y$  and  $B_z$  of the magnetic flux density  $\vec{B}$  at any point  $\vec{r} = (x, y, z)$  as follows:

$$B_x = \frac{\mu_0 I}{4\pi} \sum_{\alpha=1}^4 \left[ \frac{(-1)^{\alpha+1} z}{r_\alpha [r_\alpha + d_\alpha]} \right] \quad (2.5)$$

$$B_y = \frac{\mu_0 I}{4\pi} \sum_{\alpha=1}^4 \left[ \frac{(-1)^{\alpha+1} z}{r_\alpha [r_\alpha + (-1)^{\alpha+1} C_\alpha]} \right] \quad (2.6)$$

$$B_z = \frac{\mu_0 I}{4\pi} \sum_{\alpha=1}^4 \left[ \frac{(-1)^\alpha d_\alpha}{r_\alpha [r_\alpha + (-1)^{\alpha+1} C_\alpha]} - \frac{C_\alpha}{r_\alpha [r_\alpha + d_\alpha]} \right] \quad (2.7)$$

with

$$\begin{array}{lll}
C_1 = a + x & d_1 = y + b & r_1 = \sqrt{(a + x)^2 + (y + b)^2 + z^2} \\
C_2 = a - x & d_2 = d_1 & r_2 = \sqrt{(a - x)^2 + (y + b)^2 + z^2} \\
C_3 = -C_2 & d_3 = y - b & r_3 = \sqrt{(a - x)^2 + (y - b)^2 + z^2} \\
C_4 = -C_1 & d_4 = d_3 & r_4 = \sqrt{(a + x)^2 + (y - b)^2 + z^2}
\end{array}$$

where  $a$  is half the width of the coil in y-direction (the coil extends by  $\pm a$  in y-direction) and  $b$  is half the width of the coil in x direction.  $I$  is the (constant) current flowing through the coil. The values  $r_1 - r_4$  give the distances between each corner of the coil and the point  $\vec{r}$ . To ease notation, the x-y-plane will be denoted as the z-plane from now on.

To calculate the field of a whole coil, consisting of  $N$  windings, the calculation was done  $N$  times. The thickness of the wires  $d_w$  was accounted for in such a way that for every wire an offset is introduced, according to the thickness of the wire. This means, that the vector  $\vec{r}$  is translated by an offset and then the field is calculated. Wire crossing however, was not accounted for. Therefore, the coil simulated here consists of  $N$  individual, not interconnected rectangular coils/wire strands, placed apart according to the wire thickness, number of layers and windings per layer. Also the field was only calculated once at the middle of each wire strand. As the coils will be comparably far away from the centre of the main chamber, the small imperfections caused by these simplifications should be negligible.

To be able to calculate the field of a coil with  $N$  windings, that lies in an arbitrary plane, the above equations can still be used, but two rotations have to be performed in the following way:

First, the vector  $\vec{r}$  is rotated into the z-plane to be able perform the calculations above for a coil lying in z:

plane of desired coil	original vector	vector rotated in z
x	$\vec{r} = \begin{pmatrix} x \\ y \\ z \end{pmatrix}$	$\vec{r}' = \begin{pmatrix} -z \\ y \\ x \end{pmatrix}$
y	$\vec{r} = \begin{pmatrix} x \\ y \\ z \end{pmatrix}$	$\vec{r}' = \begin{pmatrix} x \\ -z \\ y \end{pmatrix}$
z	$\vec{r} = \begin{pmatrix} x \\ y \\ z \end{pmatrix}$	$\vec{r}' = \begin{pmatrix} x \\ y \\ z \end{pmatrix}$

if the desired coil lies in the z-plane, Eqns. 2.5-2.7 apply directly and no rotation is necessary.

Before the field is calculated, the wire thickness has to be accounted for. The different layers of wires are accounted for by tweaking the dimensions of the coil accordingly, while the wires lying next to each other in one plane are considered by translating the vector  $\vec{r}'$  as follows:

$$\vec{r}'' = \vec{r}' + \begin{pmatrix} 0 \\ 0 \\ \Delta z \end{pmatrix} \quad \text{with} \quad \Delta z = d - \left( -\frac{n_W \cdot d_w}{2} + \frac{(2n_W + 1) \cdot d_w}{2} \right) \quad (2.8)$$

where  $d$  is the distance between coil centre and the centre of the coordinate system (for coil pairs it will be the distance between the coils).  $d_w$  is the diameter of the wire and  $n_W$  is the index of one of the  $N_W$  windings (counting from zero). Thus, starting at index  $n_W = 0$ , the vector is translated by the distance  $d$ , which is simply the offset of the coil from the z-plane. Halve the thickness of the coil is subtracted, thus placing the vector at the edge of the coil and the radius of one wire is added, thus placing the vector at the centre of the outermost wire. Thus  $\vec{r}$  is translated by the distance between the centre of the coordinate system of the coil and one specific wire strand.

Now the field can be calculated at  $\vec{r}'$ . But as these results are in the reference frame of  $\vec{r}''$ , they have to be rotated back into the original frame, by reversing the original rotation of  $\vec{r}$ :

plane of desired coil	calculated field vector	field vector in reference frame of $\vec{r}$
x	$\vec{B}''(\vec{r}'') = \begin{pmatrix} B_x \\ B_y \\ B_z \end{pmatrix}$	$\vec{B}(\vec{r}) = \begin{pmatrix} B_z \\ B_y \\ -B_x \end{pmatrix}$
y	$\vec{B}''(\vec{r}'') = \begin{pmatrix} B_x \\ B_y \\ B_z \end{pmatrix}$	$\vec{B}(\vec{r}) = \begin{pmatrix} B_x \\ B_z \\ -B_y \end{pmatrix}$
z	$\vec{B}''(\vec{r}'') = \begin{pmatrix} B_x \\ B_y \\ B_z \end{pmatrix}$	$\vec{B}(\vec{r}) = \begin{pmatrix} B_x \\ B_y \\ B_z \end{pmatrix}$

Thus, the field at an arbitrary point can be calculated for one wire strand of a coil oriented in any plane.

To simulate the field of multiple coils consisting of multiple wires, the above is simply

repeated multiple times. And to simulate the field over a range of different points, all of the above is repeated for each point. This is still reasonably fast and for two coils of 100 windings each, the total magnetic field  $B_{tot} = \sqrt{\sum_i B_i^2}$  at  $10^5$  points can be calculated within a few seconds. The results of this simulation were compared to data of a similar setup [7], verifying the validity of this simulation.

With the help of these simulations, different designs were made according to the spatial constraints at hand. For each design, the field heterogeneity for the relevant region around the centre of the main chamber was calculated to be able to compare the quality of the field to other designs and to the main coil pairs. The field heterogeneity can, as in the works of others [8], be defined as:

$$h(\vec{r}) = \frac{|\vec{B}(\vec{r}_0) - \vec{B}(\vec{r})|}{|\vec{B}(\vec{r}_0)|} \quad (2.9)$$

where  $\vec{B}$  is the magnetic field vector and  $\vec{r}_0$  a reference point i.e. the centre point of the coils.

For the usual case of circular coil pairs, the highest field homogeneity i.e. the lowest field heterogeneity is achieved if both coils, have the same radius  $r$ , winding number  $N$  etc. and are placed along their common axis at a distance  $d = r$ . This configuration is then called *Helmholtz configuration*. For square coil, the same general idea applies, but the best homogeneity is achieved when the distance is [9]  $d = 0.5445 \cdot a$ , where  $a$  is the side length. As this follows the same general idea as in the circular case, it is also called Helmholtz configuration.

The field heterogeneity of circular coils in Helmholtz configuration is only slightly smaller, than that of square coils in Helmholtz configuration of comparable dimensions [10]. Depending on the way of comparing the two systems, (comparing between circumferences or between radii and side lengths) or one can even conclude that the field uniformity of square coils is better [11]. Therefore a square design was chosen originally, as compared to a circulatory design, it is the more space efficient solution for the specific application of a set of coils around a vacuum chamber.

The choice of two interlocking pairs of coils, stems again from the desire to keep the cage as small as possible. But as an interlocking square design is too large would therefore cut the optical table, the square design was formed into a similar rectangular design. It was then tested whether rectangular coils might still provide fields of high enough homogeneity. Considering rectangular coils, the field homogeneity is best for the case of square coils [12]. Thus a rectangular design using the maximum height available, as to be as close

to a square configuration as possible, was chosen. For rectangular coils the distance of  $d = 0.5445a$  will no longer provide the most homogeneous field, not least because it is no longer clear which side length  $a$  is supposed to describe. But choosing  $a$  as the longer side length,  $d = 0.5445a$  will give a good first guess and the 'correct' distance will be somewhat smaller. To calculate the spacing for which the field homogeneity in all axis is best, the field for many differently spaced coils along the xyz axes was simulated and the spacing at which the field deviation over a relevant range is lowest was found.

Finally, it has to be guaranteed, that the coil cage actually fits around all viewports of the chamber, which further limits the range of possible distances of the coils that can be considered. The resulting compensation cage presents a compromise of all the above requirements. Its coils are also wound with the same 500 $\mu$ m wire<sup>2</sup>, as the main coils, so the wires bond together stably. The bond exhibits good heat conducting properties, while the individual wires remain electrically isolated.

The dimensions of the compensation cage are as follows:

Coils	length	height	distance	layers	windings
Inner	206.4 mm	129.4 mm	78.4 mm	10	10
Outer	206.4 mm	142.2 mm	86 mm	10	10

Table 2.1: Dimensions and winding count of compensation cage

The dimensions are given for the centre of the coil. That means e.g. the actual outer length of the coils is

$$\text{length} + 2 \cdot (\text{wire thickness} \cdot \text{layers}/2) = 206.4\text{mm} + 5\text{mm} = 211.4\text{mm}.$$

The inductance of the larger coil pair is given  $L = 19.7\text{mH}$  and a field of 10.7G/A can be created and its resistance is 6.0 $\Omega$ . The field homogeneity is worst, for the smaller coil pair and along its symmetry axis. Within 1mm of the centre, the field heterogeneity is  $h = 0.003\%$ .

### 2.3.2 Design of Intermediate Coils

As mentioned above, the main coils housed inside a custom designed viewport can not be used immediately due to delays in the production of the viewport. Therefore a set of intermediate coils was designed, to replace the main coils in the mean time. These were manufactured prior to the writing of this theses and will be therefore used for testing and analysing the power supply. Their dimensions are as follows:

<sup>2</sup><https://www.elektrisola.com/en/Products/Selfbonding-Wire/Types>

Coils	mean radius	distance	layers	windings	wire	R[Ω]	L[mH]
Offset	80.228 mm	78.968 mm	8	8	500 μm	5.2	3.0
Gradient	85.016 mm	100.336 mm	10	10	1.18 mm	1.6	6.1

Table 2.2: Dimensions and winding count of intermediate coils

## 2.4 Eddy Currents

If a fast time response and alternating currents are important, one has to carefully mind *eddy currents* in the design of magnetic coils and their holders. These currents are induced in any conductor according to Faraday’s law of induction, when a changing magnetic field is present. Expressed as the Maxwell-Faraday-Equation the law of induction states [13]:

$$\vec{\nabla} \times \vec{E} = -\frac{d\vec{B}}{dt} \quad \Leftrightarrow \quad \oint \vec{E}d\vec{s} = -\int \frac{d\vec{B}}{dt}d\vec{A} \quad (2.10)$$

Thus, a magnetic field change in time induces a spatially varying electric field, and therefore a voltage  $U = \int \vec{E}d\vec{s}$ . Especially the circular holders of the coils are prone to exhibit strong eddy currents, as their geometry allows for an eddy current, directly opposite to the current flowing through the coil wires. To reduce these currents, a non conducting slit was introduced into all holders, except for the intermediate coils. Both in the copper holder of the main coils and in the aluminium holder of the compensation cage, 2mm wide slits filled with non-inductive plastic (PEEK) inserts are made. Although these should greatly reduce the effects of eddy currents in the holders, the main chamber itself is also a conductor and as it is a vacuum chamber, introducing a slit would defeat its purpose. Therefore eddy currents in the walls of the main chamber are inevitable but are reduced as much as possible, by placing the main coils (which will create time dependent magnetic fields) as close to the atoms in the centre as possible. The atoms will then ‘see’ the superposition of the magnetic field of the coils and the magnetic field of the eddy currents, so the amplitude of an oscillating field created by the coils will be in fact smaller at the position of the atoms. By continuously measuring the current through a coil and varying the applied voltage accordingly, one can reduce the effect of self-induction in the coil (see sec. 4.3). But to act against induced fields in the main chamber is not so easy, therefore prevention of eddy currents therein should be focused upon. This is done for example by electrically isolating the conducting coil holders from the main chamber with non-conductive PEEK mounts. Therefore, possible induced currents at least cannot travel from one part to another.

For the intermediate coils described above, no such slit was introduced. As a result the

effect of eddy currents can be measured easily. The current through the coil was measured with both an ampere meter<sup>3</sup> in series and with a current clamp<sup>4</sup>, which clamps around the whole coil including the mount. The for a coil with 90 windings, the measurement of the clamp should be  $A_{clamp} = 90 \cdot A_{meter}$  where  $A_{meter}$  is the measured current through the ampere meter. But in fact for an AC current in form of a 50Hz sine wave only

$$A_{clamp} = 88.5\% \cdot (90 \cdot A_{meter})$$

was measured. For currents between 50mA and 3A this result is not dependent on amplitude. When measuring the current through one wire with the clamp (i.e. not clamping around the metal holder) the results of ampere meter and clamp match.

## 2.5 Resulting Constraints on Power Supply

To generate precise magnetic fields with the coils discussed above, an equally precise power supply is needed. For the final coil design, currents of max.  $I \approx 1.5\text{A}$  are needed to create an offset field of up to 15G with the main coils and the compensation cage, and a field gradient of up to 6G/cm. As the main offset coils have a resistance of  $R \approx 5.2\Omega$ , a voltage of about  $U = R \cdot I \approx 8\text{V}$  is needed to create a continuous current of 1.5A. For the compensation cage, as it is quite larger than the other coils, about 14V are required to drive a 1.4A current through the  $9.6\Omega$  resistance of one coil pair. The gradient coils with  $R \approx 1.6\Omega$  need to be supplied with  $U \approx 2\text{V}$ . These voltages might not be large, however higher voltages allow for faster time responses of the coils (see 4.3) and therefore the supply should be able to generate much higher voltages than the above.

To be able to apply magnetic fields precisely enough to use Feshbach resonances for tuning of the dipole-dipole interaction, fields up to 15G have to be created, with a relative precision of at least  $10^{-5}$ . As the current flowing through a coil is directly proportional to the generated magnetic field, this can be translated into a relative precision of the supplied current of  $10^{-5}$  directly. This is a rather challenging constraint. For example, a 16 bit digital to analogue converter, as commonly used, will only be able to achieve a relative precision of  $1.5 \cdot 10^{-5}$  if its output was perfectly noise free. Further, the supply needs to have a good long term stability to allow for repeatable results, without needing to calibrate too often. After an unsatisfactory search of commercially available options, that fulfil these

<sup>3</sup><https://www.tek.com/en/documents/specification/keithley-model-2000-6-1-2-digit-multimeter-specifications>

<sup>4</sup>[https://www.hioki.com/global/products/current-probes/ac-current/id\\_6074](https://www.hioki.com/global/products/current-probes/ac-current/id_6074)

retirements, it was decided to custom build such a supply. The resulting design will be presented in Sec. 4 and it will be characterised in Sec. 5. The theory needed for this characterisation is explained in the following section.

# 3 Noise Analysis

## 3.1 Power Quantities and Root-Power Quantities

For a consistent discussion about noise levels and the spectrum of a signal it is often more useful to regard the power transmitted by a signal. Therefore, most definitions and calculations are done with regard of the power (spectrum) of a signal. Instead of asking which amplitude of a signal is contained within a certain bandwidth, it is more useful to calculate the power contained within a certain bandwidth.

Therefore it is very important to note whether a quantity of power (acoustic intensity, electric power) or a root-power quantity (voltage, current) is measured. For an electrical signal it is usually easiest to measure a voltage and a resistance or a current, and calculate the power from these quantities. When analysing the spectrum of a signal, amplitudes can be converted into decibels. This logarithmic unit allows for easier analysis of data over a large range of power and is consistent regardless whether a root-power quantity or a power quantity is discussed. This is due to the fact, that the conversion is different for root-power and power quantities. For a power quantity, the decibel (dB) is defined as [14]:

$$\text{ratio}[dB] = 10 \log_{10} \left( \frac{\text{signal power}}{\text{reference power}} \right) \quad (3.1)$$

For a root power quantity it is:

$$\text{ratio}[dB] = 10 \log_{10} \left( \frac{\text{signal amplitude}^2}{\text{reference amplitude}^2} \right) = 20 \log_{10} \left( \frac{\text{signal amplitude}}{\text{reference amplitude}} \right) \quad (3.2)$$

As the decibel is inherently a ratio, a reference value has to be given. Often, a voltage expressed in dB is referenced to an amplitude of 1V and is then denoted in 'dBV'. Similarly a power is usually given in 'dBm' to express that the power was referenced to 1mW of power (delivered to a load of 50Ω impedance).

As signal noise is of highest concern in this application, careful analysis of the same is important. To analyse noise, the Fourier transformation is used extensively. This is due to the fact, that the transformation allows the signal to be resolved in frequency space, such

that a frequency dependent analysis is possible. This is often needed, as every application can be associated with a certain bandwidth: a high speed application (such as digital data transmission), only ever running for a fraction of a second will not be affected by a very slow drift in the signal. But an application like the driving of magnetic coils, which serve as a low pass filter due to their relatively high inductance, will not be affected by high frequency noise. In the following, an introduction to noise analysis will be given to allow for the consequent analysis of experimental data.

## 3.2 Fourier Transformation

The Fourier transformation is defined as

$$\hat{f}(\omega) = \int_{-\infty}^{\infty} f(t)e^{-i\omega t} dt \quad \& \quad f(x) = \int_{-\infty}^{\infty} \hat{f}(\omega)e^{i\omega x} d\omega \quad (3.3)$$

where  $i$  is the imaginary number, and often the real numbers  $t$  and  $\omega$  are time and frequency.  $\hat{f}(\omega)$  can be interpreted as a function of the frequencies contained within  $f(t)$ , which is a time dependent function of amplitude. Even though the Fourier Transformation is very useful in a great variety of contexts, only the notion of time and frequency will be continued from here on. The Fourier transformation is defined as long as  $\int_{-\infty}^{\infty} |f(t)|dt$  is finite. But as one can only ever measure a time-series of discrete data points instead of the underlying continuous-time signal, the integral form of the Fourier transformation is not very handy in noise analysis. Much rather, the discrete Fourier transformation (DFT) is used, which is defined as:

$$y(k) = \sum_{n=0}^{N-1} x(n) \exp \left[ -2\pi i \frac{kn}{N} \right] \quad \& \quad x(n) = \frac{1}{N} \sum_{k=0}^{N-1} y(k) \exp \left[ 2\pi i \frac{kn}{N} \right] \quad (3.4)$$

where both  $x(n)$  and  $y(n)$  are complex numbers and  $k, n$  are indices. Thus a series of  $N$  complex numbers  $x(n)$  equally spaced (e.g.) in time, can be transformed into a series of  $N$  complex numbers  $y(n)$  equally spaced (e.g.) in frequency space, just as the Fourier Transformation does. In practice the Fast Fourier Transform (FFT) algorithm [15] is used as implemented in the `scipy.fft`<sup>1</sup> module.

To be able to analyse the noise background of a signal accurately, the following details regarding the FFT are to be noted.

---

<sup>1</sup><https://docs.scipy.org/doc/scipy/tutorial/fft.html>

### 3.2.1 Nyquist-Shannon Theorem and Aliasing

According to the Nyquist-Shannon Theorem, the range of frequencies that can be discerned in a signal is limited by the Nyquist frequency  $f_N = f_s/2$  [16], where  $f_s$  is the sampling frequency. That means, to be able to resolve a frequency  $f$  in any signal, the sampling frequency needs to be at least  $f_s = 2 \cdot f$ . Otherwise, not enough data points are recorded to assign a unique frequency to the signal. If a signal contains frequencies larger than  $f_N$ , they will be sampled incorrectly and their power/amplitudes will be assigned to frequencies below  $f_N$ . This effect is called Aliasing. The maximum discernible frequency is also called the mirror frequency, as in frequency space a frequency sweep will appear to be mirrored at the mirror frequency.

### 3.2.2 Window Functions

The DFT takes the input series to be periodic in  $N$ . This means, that to correctly perform the DFT, one would need to be very careful to measure a time series, that captures exactly an integer multiple of the period of the signal which is to be analysed. This will of course be at least impractical and often impossible before analysis of the signal. To ease this restriction a window function can be applied to the signal [17], which forms every  $N$ -length signal to have a period  $P = N$ .

An example of this can be seen in figure 3.1, where the commonly used Blackman window function was applied to a sine wave. Even though the 'recorded' signal would not be periodic (notice the jump from 0 to 1 at the end of the recorded range), the signal is made  $N$ -periodic by multiplying it with a Blackman window function, while still preserving the original frequency of the sine. The frequency spectrum of the windowed function will not exactly match that of a pure sine, but close to it. This loss in accuracy is most often made up by the much easier data acquisition. The window function multiplies every data point  $x_n$  of the series with a value  $\omega_n \in [0; 1]$ . As this reduces the overall amplitude of the window, a scaling factor associated with every window, has to be multiplied with the output to conserve to 'true' amplitude (see sec. 3.2.4).

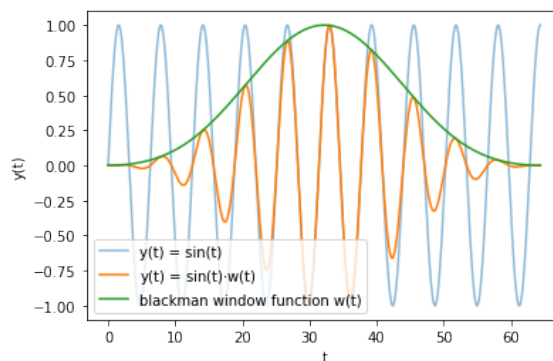


Figure 3.1: Window function applied to sine wave

Depending on the signal that is to be analysed, the window function should be chosen accordingly. In this thesis, the noise background of a current signal is to be analysed, which should ideally only contain white noise. White noise is the only case where no window function should be applied [16], as there should not be any periodicity contained within the signal.

### 3.2.3 Scalloping Loss

The FFT transforms between discrete points in time and frequency space. Therefore the FFT will only output certain equidistant frequencies which can be regarded as frequency bins of a certain width depending on the number of samples. Therefore the 'true' frequency of a signal might fall in between two discrete frequency bins and will thus cause both a broadening of the frequency peak and a diminished amplitude. This effect is strongly dependent on sampling rate, signal and the used window. To reduce this effect generally (if possible) the sampling rate should be increased.

### 3.2.4 Normalisation of Fast Fourier Transform

For any given input series of  $N$  values  $x_n$ , the FFT returns a *two-sided power spectrum*. That means the output series consists of  $N$  imaginary values  $y_n$  ranges from  $-f_{max}$  to  $f_{max}$ , with  $f_{max} = \frac{f_s}{2} - \frac{f_s}{N}$  where  $f_s$  is the sampling frequency. If the input series has no imaginary part, as will be the case for all 'real world' measurements, the output will be symmetric around 0 Hz.

As it is neither helpful to think about negative frequencies in this discussion nor is there any further information contained within the negative side of the spectrum, one can simply cut the spectrum at 0Hz and multiply any frequency  $f > 0$ Hz by a factor of two to obtain the *single-sided power spectrum*. The multiplication by a factor of two is important to conserve the true power of the whole spectrum, which allows a meaningful quantitative analysis of the data.

The FFT itself, which only generates  $N$  imaginary numbers from a series of length  $N$ , has no actual information about the sampling frequency in the real world. It will only find repetitions in the input series and convert these into another series of numbers. Thus if not only one period of the signal is recorded, but a longer signal, more repetitions will be contained within the signal and the amplitude of the correlating frequency will increase proportionally with  $N$ . Thus, for correct scaling, the result of the FFT as in Eqn.3.3 has to be divided by  $N$  [14].

Further, the effect of applying a window function has to be corrected for. To do so, two characteristic factors  $S_1$  and  $S_2$  can be calculated:

$$S_1 = \sum_{n=0}^{N-1} \omega_n \quad \& \quad S_2 = \sum_{n=0}^{N-1} \omega_n^2 \quad (3.5)$$

where  $\omega_n$  are the scaling factors of the window function.

Every window function can be associated with a certain bandwidth. This bandwidth characterises how well the window can resolve a single frequency peak. For a perfect sine wave signal, for example, which should only contain one infinitely sharp peak in frequency space, a window function will help to decrease the width (and thus the uncertainty) of the frequency peak in frequency space. But this process will never be perfect and therefore a certain broadening of the frequency peak and a reduction of its amplitude will remain. To allow to express the spectrum as a spectral density, one has to introduce the effective noise bandwidth ENBW as follows:

$$\text{ENBW} = f_s \frac{S_2}{S_1^2} \quad (3.6)$$

Finally the output of the DFT can be scaled accordingly. To calculate the power spectrum of a voltage signal  $x_n$  of length  $N$ , the DFT is calculated according to Eqn.3.3 and returns  $N/2 + 1$  values  $y_m \forall m \in [0; N/2]$  corresponding to positive frequencies. The power spectrum (PS) given in  $V_{RMS}^2$  is then given by:

$$\text{PS}_{RMS}(f_m) = \frac{2 \cdot |y_m|^2}{S_1^2} \quad \forall m \in [0; N/2] \quad (3.7)$$

The factor 2 accounts for the conversion of the two-sided power spectrum to a one-sided power spectrum. The absolute (real) value of the DFT result is squared, to calculate a power spectrum from a root-power quantity and the factor  $S_1^2$  accounts for the used window function and sampling size. In the case of no window ( $\omega_n = 1 \forall n \in [0; N]$ )  $S_1$  and  $S_2$  are both simply equal to the sampling size  $N$ . Further, the power spectrum density (PSD) given in  $V^2/\sqrt{Hz}$  can be calculated as:

$$\text{PSD}_{RMS}(f_m) = \frac{\text{PS}_{RMS}(f_m)}{\text{ENBW}} = \frac{2 \cdot |y_m|^2}{f_s \cdot S_2} \quad \forall m \in [0; N/2] \quad (3.8)$$

The amplitude of a frequency peak in the power spectrum corresponds directly to the amplitude of the input signal and is constant with sampling size  $N$ . However the broadband noise floor will scale inversely proportional with  $N$ . For the PSD however, the amplitude

peaks will inversely scale with  $N$ , but the broadband noise background will be constant over all  $N$ . Therefore, depending on the means of the discussion it is important to be able to convert from PS to PSD and back and therefore the ENBW (dependent of the applied window function, sampling size and sampling frequency) should always be calculated and noted for further discussion.

The PS and the PSD can also be converted into a *linear spectrum* expressed in V and a *linear spectrum density* given in  $V/\sqrt{Hz}$  simply by taking the square root:

$$LS = \sqrt{PS} \quad \& \quad LSD = \sqrt{PSD} \quad (3.9)$$

### 3.3 Noise Spectral Density

The PSD is most important for noise analyses, as it easily allows to display the noise spectrum and to compute the noise contribution of a certain bandwidth. As this quantity is given as  $\frac{\text{power}}{\text{frequency}}$ , the designation of density is reasonable. As all measurements in the following will be measures of voltages all the discussion in this section will focus on volts as well, but the same ideas apply to all other root-power measurements. By plotting the FFT (calculated and processed as in sec. 3.2.4) against frequency, one obtains the noise spectral density plot, which is a useful tool in noise analysis. Almost all noise sources have a certain frequency dependence. Every op amp for example has a characteristic noise spectral density associated with it. Fig. 3.2 as given in the datasheet[18] shows the noise spectral density of the AD8429 op amp, used here for current sensing. There, it can directly be seen, that the input noise density is dependent on the chosen gain of the amplifier, and that there are two different 'regions' of noise: white noise for frequencies above 100Hz and 1/f noise for frequencies below. From this graph it may be decided if the noise level of the amplifier matches the requirements.

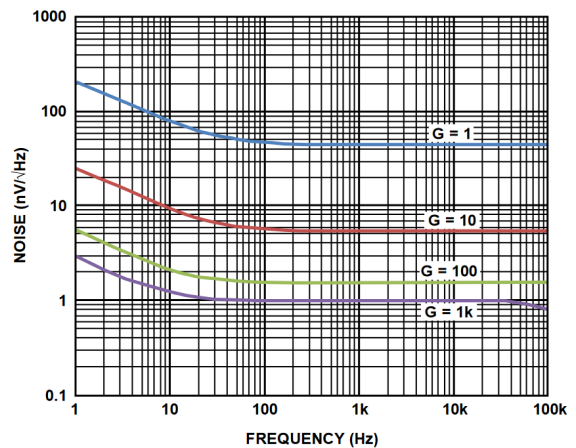


Figure 3.2: Noise Spectral Density as given in [18]

To be able to represent a wide range of frequencies it is helpful to plot the noise spectral density logarithmically and to use units of decibel.

### 3.4 Root Mean Square and Peak-Peak Noise

From the voltage spectral density, the root mean square (RMS) noise over a certain bandwidth can be calculated. Instead of calculating the RMS of the measured signal itself, this approach has the useful advantage, that a relevant bandwidth can be chosen for consideration. In the case of magnetic coils for example, because the coils can be regarded as low pass filters, noise beyond a certain cutoff frequency that might be present in the measurement can not be present in the actual current through the coil, as the time response of the latter is too slow. Therefore high frequency noise will not be present in the magnetic field produced by the coils, and can thus be discarded.

To calculate the RMS noise power over a specific bandwidth one merely has to integrate the squared voltage noise spectral density over the bandwidth:

$$RMS_{power} = \int_{f_{min}}^{f_{max}} e(f)^2 df \quad (3.10)$$

where  $e(f)$  is the spectral noise density and  $f_{min}, f_{max}$  confine the bandwidth. To translate this into a RMS noise voltage, the square root is taken:

$$RMS_{voltage} = \sqrt{\int_{f_{min}}^{f_{max}} e(f)^2 df} \quad (3.11)$$

It is often useful to think about the peak-peak value of noise, as this represents a 'worst case scenario' of noise affecting the signal. For white noise, which is inherently random, one can only give probabilities of measuring a certain peak value in a given time interval. To convert RMS to a peak-peak value, a good approximation is  $V_{pp} = 6V_{RMS}$  [19]. This stems from the assumption that the noise is Gaussian distributed and gives the width of the  $\pm 3\sigma$  interval. Thus, only 0.3% of all measurements will be outside the range of  $V_{pp}$ . However, there is no standard to define what percentage is to be used, and therefore depending on the limitations of the experiment, a fitting value has to be determined.



# 4 Design of Power Supply

## 4.1 Overview

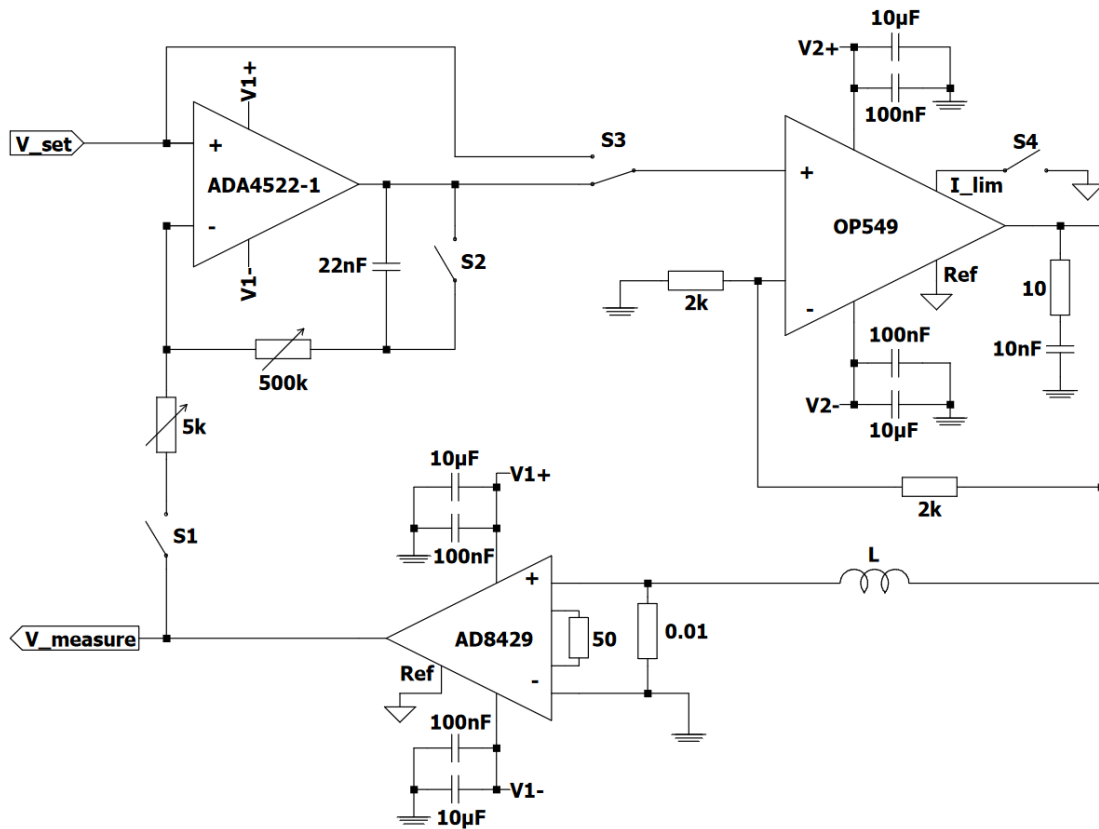


Figure 4.1: Schematic of Power Supply

Based on a paper by YM Yang et al. [20], a current controlled bipolar power supply with PI-controller was build, to match the above described requirements of precision. Namely a noise to current ratio of at least  $10^{-5}$  was set as a goal. The power supply consists of two operational amplifiers (op amp) and one instrumentation amplifier and is

comprised of basically three parts: the first part is the *current source*. It consists of a high voltage, high current operational amplifier, that receives an analogue voltage input and provides a voltage and current accordingly. Second is the *current sensing part* which consists of a highly stable resistor and an instrumentation amplifier which amplifies the voltage drop over the resistor to provide an analogue voltage measurement proportional to the current. Third, a PI-controller is implemented which receives a voltage input from the sensing part and allows for precise current setting and high frequency driving of the magnetic coils. The current source is connected to the output of the PI-controller, so it can supply a current according to the PI regulation. For an overview see Fig. 4.1.

The three parts of the power supply and their implementation is described in more detail below. To understand how this circuit works it is important to understand the functionality of an op amp, which is discussed in the following section.

## 4.2 Operational Amplifiers

An idealised operational amplifier (op amp) consists of only two voltage inputs  $U_+$  and  $U_-$ , one voltage output  $V_{out}$  and has only one parameter: the open loop gain  $G$ . Typically this gain is very large (ideally infinite) and if the op amp is used without any feedback loop, that is to say in an *open loop configuration* the output is given by  $V_{out} = G(V_+ - V_-)$ . Thus any difference between the two voltage inputs, is amplified by the large gain  $G$ . This might be used as a comparator, but the high gain constraints its usability. Most often some additional circuitry i.e. a feedback loop are required to form this device into a more functional and controllable amplifier. The most common and simple *closed loop configurations* are shown in figure 4.2. The upper schematic shows an *inverting amplifier*. Given a certain input  $V_{in}$  (which we might assume to be positive to simplify the

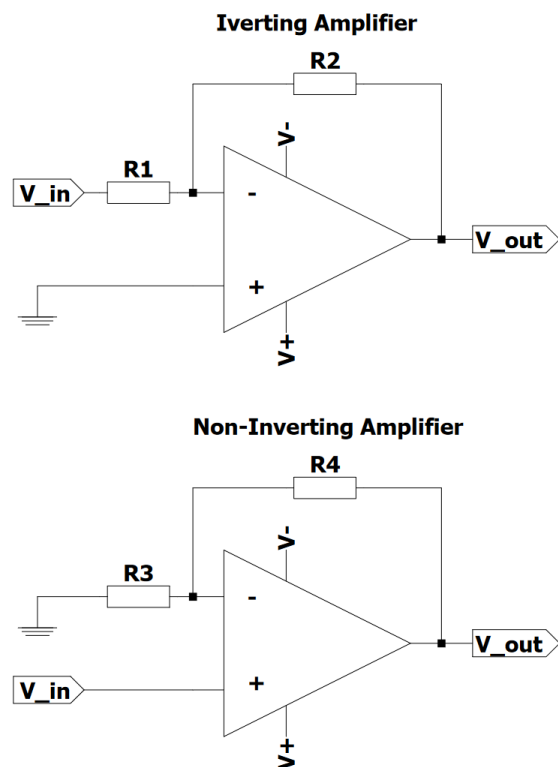


Figure 4.2: Top: Inverting Amplifier; Bottom: Non inverting Amplifier

following discussion) on the  $-$  terminal, the

op amp will amplify the difference between its two inputs. But as a feedback loop in form of a voltage divider is built around the op amp, it applies a certain voltage at its own  $+$  input, according to the chosen resistances. Thus, with a rising voltage at the output, the voltage at the  $+$  terminal is increased as well and the difference between the two terminals is reduced. Finally the difference will become zero and the voltage at the output is constant and solely determined by the resistors in the feedback loop. The amplified output of an inverting amplifier is (assuming  $G$  to be infinite)

$$V_{out} = -V_{in} \frac{R2}{R1} \quad (4.1)$$

Although the inverting amplifier inverts the difference between its input terminals, which might be a drawback in some cases, it is very useful as it allows the gain  $G$  to be set to any positive real value. Similarly, for the *non-inverting amplifier* the voltage  $V_{out}$  can be calculated as

$$V_{out} = V_{in} \left(1 + \frac{R4}{R3}\right) \quad (4.2)$$

In this case, the difference between the input terminals is not inverted, but the gain  $G \in R > 1$  can only be greater than one. All amplifiers in the power supply, presented in this thesis, work non-inverting. The alleged disadvantage of the lower bound of the Gain ( $G > 1$ ) does not matter, since each amplifier is intended to actually amplify the signal.

It is to be noted, that in both closed loop configurations presented above, the voltage at both inputs terminals is the same. Any difference between the inputs would be amplified until the difference is exactly zero. Having no voltage drop across the inputs might seem contradicting at first. As there is no voltage drop across the inputs to amplify, the signal appears to be lost. And in fact, if one terminal is grounded, one will also measure ground at the other, which is why it is often referred to as *virtual ground*. Still, the input signals and their difference are not lost, they only have to be measured outside of the feedback loop. Heuristically and by heavy personification, the op amp can be understood as a device, that 'tries as hard as it can' to keep both input terminal at the same voltage. Thus, in a closed loop configuration, it will apply an output voltage accordingly, and in an open loop configuration, it still tries the same, but the output voltage has no effect on the inputs and therefore the amplifier increases the output up to its maximum.

A further important fact is that no current flows through either input of the op amp. Any current that does flows through the output is sourced from the connected power supply. Thus the op amp has a very high impedance and can also be used as a buffer. With its high impedance the op amp is therefore well suited for current/voltage sensing,

for it will not affect the input/measurement side while providing a wide output range.

All of the above only describes the ideal case of course. In highly precise, low noise applications some further important parameters have to be accounted for. First of all, the amplifier is supplied by a power supply with the voltages  $V_{S-}$  and  $V_{S+}$ . The output of the amplifier cannot go beyond these *rails*, that is  $V_{out}$  cannot surpass  $V_{S-}$  and  $V_{S+}$ . And in fact every amplifier has a certain *output swing* specifying how close the op amp can actually be driven up to its rails. The output swing can range from millivolts to volts depending on the device. Furthermore, every op amp exhibits a certain *bias current* which specifies the current flowing through the inputs. This value also depends strongly on the chosen device from tens of fA to  $\mu$ A. The gain is of course not really infinite and tends to be frequency-dependent, which should be considered carefully when designing an amplifier. Every power supply, powering the op amp will induce a certain amount of noise. Common power supplies exhibit a high amount of noise and therefore high precision op amps are characterised by their high *power supply rejection ratio*. This value specifies to what level the power supply ripple and noise will be suppressed. Furthermore, the *common mode rejection ratio* specifies how well the op amp can amplify only the difference between two voltage inputs and not the rest of the input signals, their *common mode*.

Also, every op amp has a certain offset voltage ( $V_{OS}$ ), both at the inputs and at its output. For the devices chosen here, the value of  $V_{OS}$  ranges from 5  $\mu$ V to 5 mV and has to be accounted for by calibration. Finally a parameter most important for low noise applications has to be introduced: the *input noise density*. This parameter sums up all noise sources inside the amplifier to one noise source at its input, which is then amplified by the gain  $G$ . The amplifiers used here have a input voltage noise density ranging from  $IVND(f) = 1nV/\sqrt{Hz}$  to  $IVND(f) = 70nV/\sqrt{Hz}$  at  $1kHz$ . It is important that this parameter is as low as possible over the relevant bandwidth, as it directly adds noise to every amplified signal. Vice versa, if the noise in a system is to be reduced, its bandwidth should be limited as much as possible, because the input noise *density* has to be integrated over the bandwidth to calculate the resulting input noise (see sec. 3.4). The IVND is given at the input side of the amplifier, as this often allows for easier comparison between noise and signal. To calculate the noise at the output side of the amplifier, the IVND simply has to be multiplied by the gain. The result is called *output voltage noise density* (OVND).

All of the above parameters have to be considered carefully if high precision is important in the design. The same parameters and considerations also apply for instrumentation amplifiers, which consist of multiple (often three) op amps, and have a very similar functionality while presenting a higher input impedance and common mode rejection ratio.

## 4.3 Active Current Control

To generate a precise magnetic field, it is necessary to generate an equally precise current. Applying a constant voltage that can be set very precisely and has very low noise might not be easy already, but only applying a constant voltage will not be enough as the load of the system will not be constant over time. Especially when driving high inductance loads, such as magnetic coils, the current through the load will be strongly time dependent. Due to Faraday's law of induction (see Eqn. 2.10), as a magnetic field is built up by a current through the coil, a voltage will be induced in adverse direction. Thus the current through the coil takes a certain amount of time to ramp up. According to Ohm's law and the Maxwell-Faraday-Equation, the time dependent current can be described as:

$$I(t) = \frac{U(t)}{R} - \frac{L}{R} \cdot \frac{dI}{dt} \quad (4.3)$$

Therefore, if a coil is to be switched on fast, a higher voltage should be applied at the beginning, until the desired current is reached. Then a constant voltage according to Ohm's law has to be applied.

Also, as a coil might heat up during extended use, its resistance might change which further necessitates a measurement of the actual current at any point in time to be able to actually provide a constant, reliable and precise current and not just some constant voltage.

To allow for the input of arbitrary wave-forms and amplitudes (up to certain limits described in 5 of course), the current through the coils has to be measured constantly and compared to a given set value. This is done by amplifying the voltage drop over a small sensing resistor and comparing this signal to a given set voltage using an analogue PI-controller, as will be explained in further detail in the following chapters.

### 4.3.1 Current Measurement

The current through the load (i.e. the coils) is measured as a voltage drop over a high precision  $10 \text{ m}\Omega$  *sensing resistor*. This foil resistor by Vishay Precision Group is designed such, that its resistance is only very slightly temperature dependent. It is specified [21] that the resistance of  $10 \text{ m}\Omega$  ( $\pm 0.1\%$ ) increases by only  $2.0 \text{ ppm}/^\circ\text{C}$ . Because of the low resistance, the resulting voltage drop over the resistor and thus the power dissipated by it will be equally small. This property in addition to the low temperature dependence of the resistor result in a highly constant resistance and therefore allows for stable current sensing after an initial calibration.

The currents used to generate the magnetic fields in the experiment will be in the order of 1A. According to Ohm's law, for a 1A current the voltage drop over the resistor will be only  $U = R \cdot I = 10\text{mV}$ . To achieve a signal to noise ratio of  $\sim 10^5$  that would require an accurate measurement of 100nV, which is not easy and prone to interference from noise sources within the laboratory. Therefore the small voltage drop over the resistor is amplified by the instrumentation amplifier AD8429 (called *sensing amplifier* henceforth) with a gain of  $G \approx 120$ . As a result only an accurate measurement of about 10 $\mu\text{V}$  is necessary, which is much easier to accomplish.

A single resistor can be used to set the gain of the sensing amplifier. To achieve a gain of 120 a 50 $\Omega$  (Vishay Precision Group) precision resistor is used, which provides a similarly low temperature coefficient[22] of  $\pm 2.5\text{ppm}/^\circ\text{C}$ . It is important to use a highly precise resistor for gain setting of course, as its drift will affect the gain and with it the output of the sensing amplifier.

A analogue voltage input source that can provide a voltage signal with a signal to noise ratio of  $10^5$  is needed of course. To be able to fully use the voltage range of the input (and therefore maximise precision) the gain resistor should be chosen such, that the maximum current that is expected/allowed, is sensed as a voltage signal matching the full range of the analogue input source. In this prototype of the power supply a 50 $\Omega$  resistor was used, because the resulting gain of 120 in the sensing amplifier translates a 1A current (roughly) into a 1.2V voltage, which seems reasonable and allows for flexible testing with the devices at hand.

To improve the precision of the sensing amplifier, bypasses consisting of two capacitors in parallel were connected at each voltage supply terminal (V1+ and V1- in fig. 4.1). The capacitors with 100nF and 10 $\mu\text{F}$  respectively, greatly help to reduce ripple and noise pickup from the power supply. The smaller capacitor should be placed as physically close as possible to the operational amplifier, while the larger one should be placed closer to the power supply, but wire/line length is not as critical in this case.

The sensing resistor comes with four connection terminals, which allows for *four wire sensing*. Having four connections on a resistor (one pair 'before' and one pair 'after' the resistor) allows to separate current carrying lines from sensing lines. By doing so, the voltage drop over the current carrying lines and their connections to the resistor is not measured, but only the voltage drop over the resistor itself. As the current flowing through the inputs of the sensing amplifier is negligible, so is the voltage drop over its connections with the resistor (Ohm's law). This means, that the length of the connection lines from the resistor to the sensing amplifier inputs is not as critical. Therefore, four wire sensing allows for a much more precise measurement of the voltage drop.

### 4.3.2 PI-Control

After a sufficiently accurate measurement of the current, that is running through the coil at any time is made, this measurement needs to be compared to the desired value and, if necessary, the current needs to be corrected. This is done with the help of a PI-controller. This controller, which is a simpler version of a PID-controller, is able to adjust its output depending on both a desired set voltage  $V_{set}$  and the actual value of a measured voltage and will be explained in further detail below.

A PID-controller is a closed-loop feedback system that adjusts its output depending on both a set-point and a feedback loop. The feedback loop contains information of the actual value of the output signal, such that a difference between actual value and the set-point can be calculated. In the practical sense a PI controller as implemented here is a device, the *actuator*, that calculates the difference between a set voltage  $V_{set}$  and a feedback voltage  $V_{fb}$ , that gives information about the *process*. The result is called the error  $e(t) = V_{set} - V_{fb}$ . The output is then dependent on the parameters of the controller of which it has two: the proportional gain parameter P, the integral gain parameter I. A complete PID-controller also has a differential gain parameter D. The whole system, i.e. the actuator which is driving the process, is called the *plant*.

The PI controller will use these two parameters to calculate an output dependent of the error  $e(t)$  in the following way[23]:

$$U_p(t) = Ge(t) + U_b \quad (4.4)$$

$U$  is called the control variable (in this case the voltage output),  $G$  is the proportional gain and  $U_b$  is a bias value which might be part of the system (in this case a bias voltage in the op amp for example (see sec. 4.2)) and will be omitted in the following as any offsets that will accumulate in the circuitry will be compensated by calibration.

As the proportional part of the PID controller outputs a voltage  $U_p(t)$ , the value of the feedback loop will change and the error  $e(t)$  will become smaller (normally). The feedback loop of the PID controller should be much faster than the driven load so that while the feedback signal changes, the controller can vary its output simultaneously. This means, that the proportional part alone will change its output continuously until an the error is exactly  $e(t = \infty) = (U(t) - U_b)/G$ . In this case an equilibrium is reached and the output will be constant, while having a constant offset of  $e(t = \infty)$ . To remove this offset the integral part of the controller is used. This integrates the error of the signal over time and

varies the output accordingly in the following way:

$$U_i(t) = \frac{G}{T_i} \int_0^t e(\tau) d\tau \quad (4.5)$$

Therefore any constant offset will cause the integral part to vary the output until the offset is zero. If the application requires a stable and precise output, the I-part is necessary. If a fast time response is needed, a differential part might be used. The output if the D-part is as follows:

$$U_d(t) = G \cdot T_d \frac{de(t)}{dt} \quad (4.6)$$

This means the differential part increases its output when the signal changes and therefore increases the rate of any change. If this behaviour is not countered by the I-part, the system will be driven out of stability. As the frequency response of the herein tested coils is good enough for the purposes of the dysprosium experiment with just a proportional and integral controller and as stability of the signal is of highest concern, no differential controller was implemented. (see sec. 5.1 and sec. 5.4)

A PI-controller can be implemented as an analogue device or via a digital computation. Here, an analogue design was chosen for different reasons. First, the design presented below consists of only four components and is thus not only easy to implement, but having less parts should in principle mean fewer sources of noise affecting the system. Also, the time response of such an analogue design should be orders of magnitudes faster than that of the magnetic coils and will therefore be sufficient

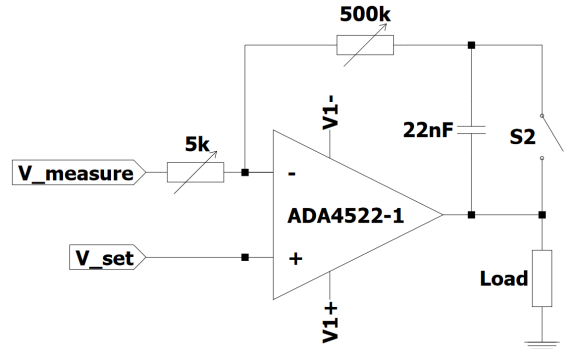


Figure 4.3: Schematic of the PI-controller

to control the coils accurately. Implementing a digital PI on the other hand, would necessitate an analogue to digital converter (ADC), a microcontroller and a digital to analogue converter (DAC), all of which could contribute to the noise accumulating in the system.

To implement the PI-controller, an op amp (ADA4522-1) was used in combination with two gain resistors and one capacitor, a schematic of which can be seen in Fig. 4.3. To allow for manual adjustment of the PI parameters, two potentiometers (5kΩ and 500kΩ) are used. This is a compact design, combining the proportional and integral part in one. To allow for testing and tuning (see sec.5.1) a switch was installed, bridging the

capacitor. With this switch open, only a proportional controller remains and the tuning method described in sec. 5.1 can be used. Two further switches (S1 and S3 in Fig.4.1) were installed, with which the PI-controller can be decoupled from the rest of the circuitry to allow for testing and analysis.

Following the example of Yang et al.[20] the AD4522-1 op amp was chosen for the PI-controller, because of its low offset voltage, its extremely low offset voltage drift and its low voltage noise density, even below 1 Hz. In detail, the datasheet[24] states, that the offset voltage of 5 $\mu$ V drifts by max 22nV/ $^{\circ}$ C. Together with the very low peak-peak-noise of typically 117nV from 0.1Hz to 10Hz, this makes the ADA4522-1 especially suitable for PI-control, as most op amps have a high amount of 1/f noise at low frequencies (below 100Hz) and can therefore not give a stable and reliable output over longer time periods. All together, the low frequency noise and offset is about halve the specified level of  $10^{-5}$ , so a stable signal control can be expected.

The potentiometers and the capacitor need not be precise and may well drift with temperature, as the drift of their values will only slightly change the PI-parameters. This is not very concerning as these parameters are not set extremely precisely and they only affect the behaviour of the PI-controller, but not the stability of the signal directly. For the analysis below, the PI amplifier and the sensing amplifier are supplied with  $\pm 14$ V by a HAMEG HMP4040 power supply<sup>1</sup>. The two pairs of bypass capacitors described for the sensing amplifier are therefore connected to both the sensing and the PI amplifier and help to reduce power supply noise in both. A further small capacitor could be used even closer to the PI amplifier, but this was not done due to spacial constraints. Further noise from the power is suppressed by the sensing amplifier with a power supply rejection ratio (PSRR) of 160dB.

Combined, the current sensing over a 10m $\Omega$  resistor and the PI-controller enable the input of an arbitrary voltage, which is directly proportional to a current through the coils. The current is not only controlled, very precisely but the PI-controller also allows for high frequency driving of the coils (see sec. 5.4).

### 4.3.3 Current Source

Finally the output of the PI amplifier is connected to the high current operational amplifier OPA549 [25]. While having a low noise level with an input voltage noise density  $IVND=70\text{nV}/\sqrt{\text{Hz}}$  and current noise density  $CND=1\text{pA}/\sqrt{\text{Hz}}$  it is capable of an 8A continuous

---

<sup>1</sup>[https://www.rohde-schwarz.com/us/products/test-and-measurement/dc-power-supplies/rs-hmp4000-power-supply-series\\_63493-47360.html](https://www.rohde-schwarz.com/us/products/test-and-measurement/dc-power-supplies/rs-hmp4000-power-supply-series_63493-47360.html)

output and 10A peak. Further, with a slew rate of 9V/ $\mu$ s the 'power amplifier' allows for fast switching and greatly outperforms the timescale of the coils.

It is powered by two Delta Electronika ES030-5 supplies, which can together provide  $\pm 30V$  and  $\pm 5.5A$ . It acts as both a current source and sink, which enable fast switch on and off times of the coils. For an IC component, the OPA549 is rather large and has a metal tab which allows it to be screwed in place. This tab is internally connected to the V- terminal, but should not be used to conduct any current. But as the device can heat up significantly during use, it should be placed upon a heat sink. For a DC output current  $I_{out}$  the power dissipated by the op amp can be calculated as[26]:

$$P = I_{out} \cdot V_{CE} \quad (4.7)$$

where  $V_{CE}$  is the voltage over the output transistor. If the output voltage is positive/negative,  $V_{CE}$  is equal to the difference between the positive/negative supply voltage and the output voltage:  $V_{CE} = |V_S| - |V_O|$ . For AC signals the power consumption can be estimated over the RMS value of the current. For a sine wave with a peak peak amplitude of  $I_{pp} = xA_{pp}$ , the RMS value is  $I_{RMS} = x/(2\sqrt{2})$ . The power of this sine is equal to the power of a DC current with amplitude  $I_{DC} = I_{RMS}$ . This might be used as an approximation for all sinusoid signals.

As the magnetic coils have a only small resistances the voltages needed to drive the necessary currents is also rather small. But to allow for fast switching or high frequency driving of the coils, higher voltages are needed and the device heats up significantly. All frequency-dependent measurements below were done with the supply voltages set to  $\pm 30V$ . Driving a 0.8A<sub>pp</sub> sine wave therefore results in a power of  $P = 0.8A/(2 \cdot \sqrt{2}) \cdot 30V = 8.5W$ , which requires the power amplifier to be mounted on a heat sink, but passive cooling is sufficient. Still, beyond the scope of this prototype build, a proper heat analysis has to be done and the mounting and housing of the power amplifier and the remaining circuitry have to be designed carefully. Even though the power amplifier might be able to operate at temperatures as high as 160°C, the current sensing part should not be allowed to heat/cool more than  $\pm 5^\circ C$ , as this would result in a 10ppm increase of the resistance of the sensing resistor, and therefore a deviation of its calibration in the order of  $10^{-5}$ .

A built-in thermal shutdown will disable the output automatically at a temperature above 160°C and will only re-enable as the temperature cools below 140°C. The E/S pin provides information about the thermal status of the op amp, so it could be monitored or indicated by an LED light and further allows to enable/disable the output by driving the E/S pin high/low. Both of these functions were not implemented in the prototype

version presented here. The OPA549 also provides a current limiting pin. Dependent on the applied voltage, the output current can be limited between  $\pm 10\text{A}$  (full range) and  $0\text{A}$ . To be able to switch off the output, a switch was installed, connecting the reference pin (Ref) and the current limiting pin (I\_lim) as can be seen in figure 4.1. If I\_lim is grounded, the output current is maximal and if it is left open, the output current is disabled. This allows for safe and fast testing, as the output can simply be disabled with one switch, if the input voltage source for example is disconnected, without the need of turning off the whole power supply.

According to the application information in the datasheet[25], again two pairs of bypass capacitors were installed. As recommended, a ceramic capacitor ( $0.1\mu\text{F}$ ) and a tantalum type capacitor ( $10\mu\text{F}$ ) were used. Further, for high inductive loads an output compensation stage was recommended and implemented in form of a  $10\Omega$  resistor followed by a  $10\text{nF}$  capacitor in series, which were connected parallel to the load (see fig. 4.1). This serves as a snubber and helps to stabilise the output. As, especially for the bypass resistors, lead length is critical and the prototype was built without a custom designed printed circuit board (PCB), the bypass and output stage compensation were soldered to the terminal pins of the power amplifier directly. This improved stability greatly, compared to wires of about  $40\text{cm}$  length soldered to the pins and then connected on a breadboard.

To set the gain, two  $2\text{k}\Omega$  resistors were used, resulting in a gain of  $G = 2$  (see Eqn. 4.2). These were also soldered onto the output, reference and minus input terminal pins directly. Standard resistors can be used here, as the gain neither has to be set very precisely, nor does it have to be very stable. Any drift in the gain would be cancelled out by the PI-controller.

The reference pin (Ref) allows to set a reference voltage for the power amplifier. One has to be careful to avoid ground loops when connecting Ref to ground. The best results could be achieved if a *signal ground* and a *power ground* were established. That means, connecting all grounds that serve as a reference and where typically no current is conducted at one place and having a separate physical location (as close to the ground of the power supply as possible) to conduct current. These different ground types are indicated in fig. 4.1 with a triangle shape for signal ground and the common ground symbol for power ground.

This practice reduces noise significantly and together with the short-lead bypass capacitors, the influence of interfering signals (pickup of stray electromagnetic fields; 50Hz mains hum) is nearly completely eliminated (see 5.5).

Finally, a small metal case was built around the sensing and PI part, to allow for further shielding of electromagnetic interference. The input to the PI-controller is given

via a BNC cable and the voltage output of the sensing amplifier can also be monitored over a BNC connection. The power amplifier is screwed onto a heat sink outside of the metal case, and its reference, current limit and input terminals are connected by cables of about 30cm length, with soldered connections at both ends.

# 5 Experimental Results

## 5.1 Optimisation of PI Parameters

Before any measurements can be made, the PI-control has to be optimised. To do so, the Nichols Ziegler method was used [23].

The approach of Nichols and Ziegler examines the behaviour of the control sequence when only the P-controller is active and calculates the optimal parameters accordingly. Because stability is of higher concern than the time response of the system, which is already fast enough, only a PI-controller is used. To be able to measure the response of the system, when only a P-controller is active, a switch was installed, parallel to the capacitor in the PI-controller (see switch 'S2' in fig. 4.1). As the PI-parameters are dependent on the whole plant (both actuator and process) the parameters are dependent on the coils, which are used and therefore have to be tuned specifically for each application.

After the whole setup is connected and the switch S2 is closed, the gain of the P-controller is steadily increased until the actuator begins to oscillate. The gain at which the oscillations settle only very slowly, is called  $G_{Rkrit}$  and is recorded. The period of the oscillations is  $T_{krit}$  is also measured. Then the parameters of the PI-controller can be calculated as follows:

controller type	$G_R$	$T_i$	$T_d$
P	$0.5G_{Rkrit}$	-	-
PI	$0.45G_{Rkrit}$	$0.85T_{krit}$	-
PID	$0.6G_{Rkrit}$	$0.5T_{krit}$	$0.12T_{krit}$

Table 5.1: PID parameters following Nichols-Ziegler method as in [27]

In practice however, due to their high inductance, the magnetic field coils present a very stable system. Therefore, it is not easy to get their current to oscillate. If the highest gain is selected for the P-controller and a step function with an  $\sim 1.6\text{A}$  amplitude is applied, the current through the magnetic coils oscillates only about 10 times before settling to a constant current. That means, the open loop gain of the here used ADA4522-1 is just not

high enough to cause instability in the plant. Thus the control variable is too restricted to use the Nichols Ziegler method. As some oscillations in the current can be observed, the open loop gain of the PI-amplifier seems to be close to the optimal value and one might try to use it as an approximate value for  $G_{Rkrit}$ . However trying to calculate the optimal PI parameters according to Nichols and Ziegler is fruitless for the following reason: The gain of the PI amplifier (compare Fig. 4.3) is calculated as in Eqn. 4.2:

$$V_{out} = V_{in} \left( 1 + \frac{R4}{R3} \right) \quad (5.1)$$

To set the maximum gain of the amplifier, the potentiometer R3 has to be set to  $R_3 = 0\Omega$ . In reality, a resistance close to  $0\Omega$  can be set and the gain is nearly independent of the resistance of the potentiometer R4 in this case. But when the potentiometer R3 is set to  $0\Omega$ , the resistances of the solder connections and lines connecting the potentiometer with the amplifier have a similar value as the resistance of the potentiometer itself, and therefore it is difficult to measure the actual resistance. Further, if the gain of the PI-controller is to be set to  $0.45G_{Rkrit}$  (according to Tab. 5.1), one would need to adjust the resistance of the potentiometer R3 to  $1/0.45$  times its very small value, which is not feasible in practice.

However, Åström and Hägglund[23] describe a PI-controller, well tuned according to Nichols and Ziegler. They describe, that for many industrial purposes an overshoot  $o$  of roughly 8-10% a decay ratio  $d = 1/4$  are exhibited by well tuned PID-controllers. The overshoot is defined as:

$$o = \frac{I_{peak} - I_{set}}{I_{set}} \quad (5.2)$$

where  $I_{peak}$  is the value of the peak current and  $I_{set}$  the set value, which is achieved after a long time. The decay ratio is the ratio between the height of the first and second oscillation. Ideally, both the overshoot and the decay ratio should be minimised, but in reality this is only possible to a certain extend of course.

It is possible to try and adjust the parameters of the PI-controller by hand, until these characteristics are exhibited. After all, the method by Nichols and Ziegler and all related methods are merely used to quickly find a good set of parameters. But they are neither perfect for every plant, nor is it impossible to find similar parameters by hand. Thus, as the Nichols-Ziegler method cannot be applied, the parameters were set by hand for each set of coils.

To do so, most importantly, the integral part of the PI-controller needs to be able to eliminate any offset between the set value and the output, to allow for very precise current control. The proportional part is then set, to achieve a fast time response of the coils. As

the control variables are too restricted, the result might not be perfect, but give a good estimation of a well tuned PI-controller. The resulting time response of the coils will be discussed in further detail in Sec. 5.3 and Sec. 5.4.

For the purpose of the following analysis, the PI-controller with the here found parameters might be sufficient. But for the later use of this power supply in the dysprosium experiment the PI-controller should be further approved upon. Even though this improvement is beyond the scope of this thesis, following options could be considered:

First, one could simply replace the ADA4522-1 by an op amp with equally low drift and offset voltage, but with a higher open loop gain. While this is possible, it just requires the existence of such an op amp and the need to find it. Alternatively, it is possible to implement two op amps in a secondary-primary ('master-slave') configuration, where the primary is actually responsible for performing the PI-control calculations and the secondary merely copies the voltage output of the master. The combined output of this configuration is therefore double the maximum current and voltage output of just one op amp. Combined they can therefore also double the gain, which should be sufficient for a wide variety of loads, similar to the coils used for testing in this thesis. In practice this can of course have drawbacks. For example both offset voltages and noise of both these amplifiers are also added.

'Simply' selecting a higher gain amplifier would therefore be the better option, but the primary-secondary configuration does present a very possible option.

## 5.2 Current Sensing

Next, the current sensing part of the power supply has to be tested and calibrated, as only then a quantitative analysis is possible. The sensing part, consisting of a high precision, low drift  $10\text{m}\Omega$  resistor and an AD8429 instrumentation amplifier (as described in Sec. 4.3.1, gives a voltage output proportional to the current through the resistor, which is connected in series to the load. Because of the non-zero offset voltages and currents of all op amps involved, it is possible, that a certain voltage offset

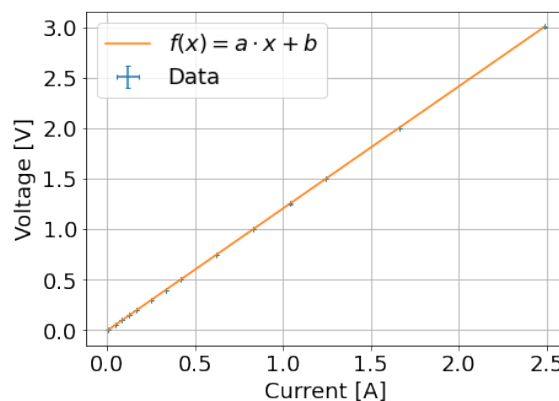


Figure 5.1: Voltage output of sensing amplifier compared to measured current

is observed. Further, as the voltage measurement is only proportional, the factor of proportionality has to be determined.

To do so, a coil is connected to the power supply as load and a Keithley 2000 6.5 digit multimeter<sup>1</sup> is connected in series to the coil. Different DC voltages are applied as an input (by a HP 33120A Arbitrary Waveform Generator<sup>2</sup>) and the resulting output voltage of the sensing part is monitored simultaneously with the measured current through the Keithley multimeter. To test for any offset current in the Keithley multimeter, its inputs were shorted and a current of 140nA was measured. This is negligible, for the purpose of this measurement, as the current noise level for all other measurements was  $\geq 10\mu\text{A}$ . The current in the multimeter is plotted against the voltage output of the sensing part in figure 5.1. As expected the relationship is highly linear and by fitting a function  $f(x) = a \cdot x + b$  to the data (which can also be seen in fig.5.1) the following parameters can be determined:

- Proportionality factor  $a = (1.2093 \pm 0.0010)\Omega$
- Offset  $b = (-2.47 \pm 0.18)\text{mA}$

These fit the expectation closely, as the sensing resistor has a value of  $10\text{m}\Omega$  and the voltage drop is amplified by an instrumentation amplifier with gain  $G = 120$ . Thus, a 1A current through the resistor should result in a 1.2V output. With these parameters, the voltage output of sensing part can be converted to a current by performing the simple rescaling:

$$x_A[\text{A}] = \frac{x_V[\text{V}]}{a[\Omega]} + b[\text{A}] \quad (5.3)$$

In the following, this conversion will be used to calculate currents measured by the sensing part of the power supply.

## 5.3 Risetime and Faltime

As described above (Sec. 5.1) for tuning of the PI parameters and to characterise the response of the system to fast switching, a step function with an 0.8A amplitude is applied. The resulting current through the coils is recorded with and without active PI-control. Solely for the purpose of testing, two more switches were installed (see 'S1' and 'S3' in

<sup>1</sup><https://www.tek.com/en/documents/specification/keithley-model-2000-6-1-2-digit-multimeter-specifications>

<sup>2</sup><https://www.keysight.com/de/de/product/33120A/function-arbitrary-waveform-generator-15-mhz.html>

fig.4.1), which allows the input signal to be processed by the PI-controller or to be given as a set voltage to the power amplifier directly.

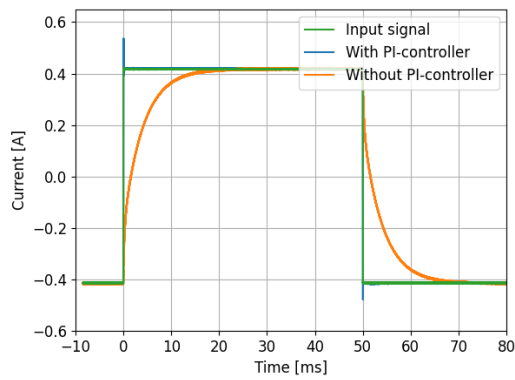
It has to be noted, that the PI-controller regulates the signal such, that the set voltage and the output of the sensing part are the identical. That means, depending on the load, the voltage output of the PI-controller might be very different from its input. If the PI controller is isolated by the switches S1 and S3, and the set voltage is used directly as the input for the power amplifier, it will amplify the input with a gain  $G = 2$  no matter what the resulting output current or voltage drop over the resistor is. As an example, if a  $R = 10\Omega$  load is connected and the set voltage is  $V_{set} = 1V$ , then the output of the PI-controller will be around 6V. This will be amplified by the gain of the current source, which will then apply a 12V voltage to the load, resulting in a 1.2A current through the sensing resistor. The amplified voltage drop in the sensing part will then be around  $1.2 \cdot 0.84V \approx 1V = V_{set}$ . Without the PI-controller on the other hand, the current source will directly amplify  $V_{set}$  and the resulting current will be around 200mA.

Thus, if one is to compare the time response for a step function, with and without PI, the set voltage has to be changed between measurements such that the constant current output is the same. This is done for the measurements without PI-controller, simply by measuring the amplitude of a DC current with an oscilloscope and varying  $V_{set}$  until the desired amplitude is reached.

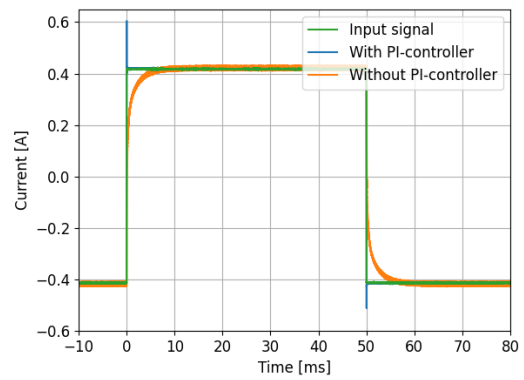
Figures 5.2a and 5.2b show the current, flowing through the coil when a 10Hz square wave with a  $1V_{pp}$  is applied as set voltage  $V_{set}$ .  $V_{set}$  is translated into the corresponding set current and plotted as such.

One can clearly see that the PI-controller helps to improve the time response of the coils. As expected from Eqn. 4.3, without any PI regulation the current rises and falls in an exponential matter. When the PI-controller is turned on, it regulates the applied voltage  $U(t)$  and the resulting current follows the set value closely. Figures 5.2c and 5.2d show a zoom of the figures above. Only the set value and the PI-controlled current are visible in the zoomed in graphs, as the time response without PI-control is too slow to be visible.

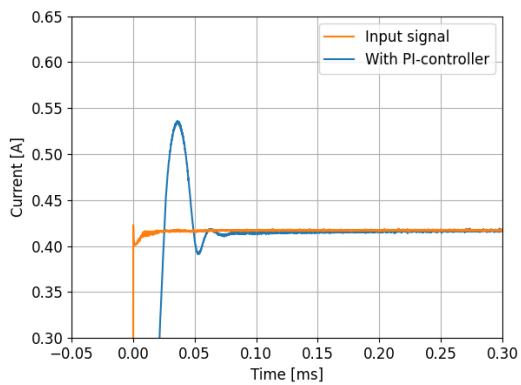
To be able to compare the time response with and without PI-control, the settling time  $t_s$  is measured and the overshoot  $o$  where measured.  $t_s$  describes the time it takes until the respective current settles within 1% of the set value, without leaving that range again. That means in case of an overshooting signal,  $t_s$  describes the time, when the initial overshoot and consequent oscillations have subsided and the signal remains within 1% of the set value. The resulting values can be found in table 5.2. The PI-controller causes a sharp increase of the current and a significant overshoot and a reduction of the settling time



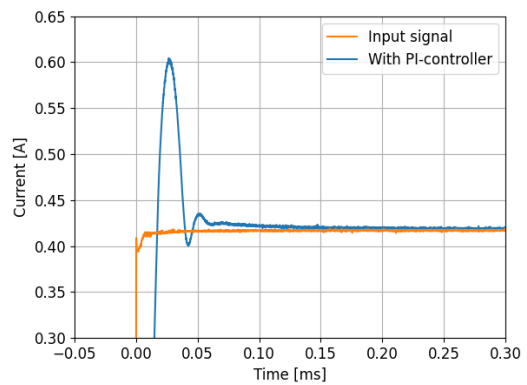
(a) Step Response Gradient Coil



(b) Step Response Offset Coil



(c) Step Response Gradient Coil (Zoom)



(d) Step Response Offset Coil (Zoom)

Figure 5.2: Comparison of step responses with and without PI-control

is observed. For both the rising and the falling edge of the step response, the overshoot was measured and the results are summarised in table 5.2 as well. The PI-parameters were tuned to improve the time response of the coils. Therefore the overshoot is higher often higher than the 10% specified by Åström and Hägglund as described above. As the system is highly stable, the decay ratio is very small, even though the overshoot might be large. Therefore the plant exhibits next to no oscillations even for an overshoot of up to 22.7%. Whether the effect of such a significant overshoot is negligible or detrimental, has to be decided specifically for each application. On the falling flank, the overshoot is lower in all measurements and the settling time is lower in most cases. This asymmetric behaviour of the plant might stem from the fact, that the output swing of the power amplifier is not symmetric. For an output of 2A, the maximum voltage output of the OPA549 is  $(V_+ - 3.2)V$  and  $(V_- + 1.7)V$ . Therefore it is to be expected, that the power amplifier does not behave symmetrically to some degree. But as the power amplifier should not go up to its rails if no PI-control is active, this result is still surprising.

It has to be noted further, that while the settling time of the gradient coils of less than  $100\mu s$  is quite good, the settling time for the offset coils is slower, even though their time response without the PI-control was better. This can be explained, as the integral gain of the PI was not set high enough to allow for a fast compensation of the offset error.

	$o$ (rising)	$o$ (falling)	$t_s$ (rising) [ms]	$t_s$ (falling) [ms]
Gradient coils without PI	- - -	- - -	19.82	18.85
Offset coils without PI	- - -	- - -	7.25	6.89
Gradient coils with PI	14.7%	7.3%	0.078	0.067
Offset coils with PI	22.7%	11.7%	0.123	0.135

Table 5.2: Rise and Fall Times of Intermediate Coils

## 5.4 Frequency Response

To investigate the frequency response, a sine wave with an equivalent peak peak current of 0.827A was given as a set value for frequencies ranging from 1Hz-100kHz. The amplitude of the resulting current through the gradient and offset coils was measured for each frequency and is plotted in Fig. 5.3 for the case of no active PI-control, while Fig. 5.4 shows the same with active PI-control.

One can see at first glance, that the PI enables the driving of higher frequency currents as expected. In detail, however the results are rather surprising. For a set voltage in form

of a sine wave with constant amplitude and varying frequency, the corresponding current can be calculated according to the (complex) impedance of the coil. The impedance of a coil is given by

$$Z = R + i\omega L \quad (5.4)$$

and consists of the resistance  $R$  of the coil and its inductance  $L$ .  $\omega$  is the frequency of the sine and  $i$  is the imaginary unit. The current  $I(t)$  flowing through this impedance when a voltage  $U(t)$  is applied, can be calculated according to Ohm's law:

$$I(t) = \frac{U(t)}{Z(t)} \quad \& \quad |I(t)| = \frac{|U(t)|}{\sqrt{R^2 + \omega^2 L^2}} \quad (5.5)$$

Only the magnitudes  $|U(t)|$  and  $|I(t)|$  of the complex voltage and current and their phase delay  $\theta$  are available to measurement. If the applied voltage amplitude is constant, the expected frequency dependence of the current amplitude is only frequency dependent, as  $R$  and  $L$  are constant. The latter two can be estimated for the used coils, so that the frequency dependent current amplitude can be calculated. The result can be seen in Fig. 5.3 in form of the two solid lines. The blue line shows the expected frequency dependence for the gradient coils, while the orange corresponds to the offset coils. Both the resistances and the inductance used for these calculations, where calculated according to the used wire, number of turns etc. The calculated resistances can be verified by measurement with a multimeter<sup>3</sup>. The results deviate by less than 6%.

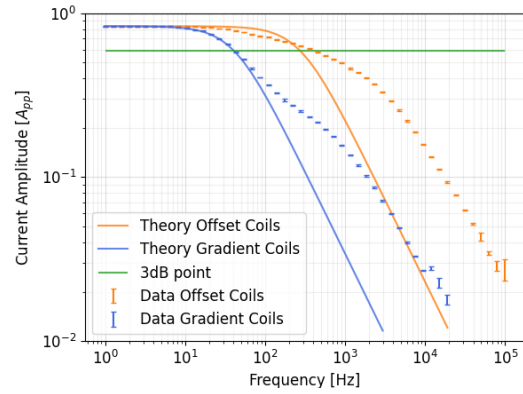


Figure 5.3: Frequency dependence without PI-control

The measured frequency dependence is shown in Fig. 5.3 as the orange (offset coils) and blue (gradient coils) data points with error bars indicating 1 standard deviation  $\sigma$ . It is clear, that theory and experiment deviate significantly. For higher frequencies, the current amplitude is actually higher than expected. While the measurement with the gradient coils matches the theory at least up to  $\sim 70\text{Hz}$ , the measurement of the offset coils deviates even before that. It was tried to estimate the inductance from the measurements, by using

<sup>3</sup><https://www.tek.com/en/documents/specification/keithley-model-2000-6-1-2-digit-multimeter-specifications>

linear regression to fit Eqn. 5.5 to the data. For the offset coils however, no sensible fit could be achieved, while for the gradient coils it is only possible to model the first  $\sim 20$  data-points with Eqn. 5.5. The resulting inductance is  $L_{gradient} = (5.30 \pm 0.08)\text{A}$ . This is 14% smaller than the calculated value and the two results deviate significantly. To better match the data, also the resistance was given as a free parameter for a linear regression or the measured resistance was used instead of the calculated value. However, this does not suffice to explain the observed data.

It might be possible, that the coils exhibit a small capacitance, which might add to the impedance. However, the impedance of a capacitor is given by  $1/(i\omega C)$  and might thus only reduce the low frequency current amplitudes, while its effect should become smaller for higher frequencies. As no such behaviour can be found in the data, a non-zero capacitance of the coils cannot explain the frequency dependence. A frequency dependence of the resistance of the wire might cause a certain deviation from the theory, however the resistance would have to be significantly frequency dependent for frequencies as low as 100Hz, which does not seem plausible.

Further, one might try to calculate the the inductance of the coils by looking at the phase delay of voltage and current. This should be described by

$$\Delta\Phi = \arctan\left(\frac{L}{R}\right) \quad (5.6)$$

However, this behaviour can not be seen in the collected data and no reasonable inductance can be calculated with this approach.

Even though no satisfying explanation of the measured data was found, in a similar thesis [28] the frequency dependence of electromagnetic coils was measured and a similar frequency dependence was found. For frequencies above  $\sim 500\text{Hz}$  an increase of the amplitude, compared to the fit can be observed in that thesis. However no conclusive explanation is given.

The 3dB frequency of the gradient coils is estimated from measurement to be 41Hz. For the offset coils it is roughly 416Hz.

The same measurement of the frequency dependent current amplitude was repeated, but with an active PI-controller. In this case, it is not as easy to calculate the frequency response from theory, as the voltage  $U(t)$  will now be the output of the PI-controller. This output can vary greatly depending on the PI-parameters, the frequency and the set voltage and can not be calculated easily. Still, the frequency response can be split into two. In the first regime i.e. for frequencies up to  $\sim 10\text{kHz}$  in Fig. 5.4, the PI-controller and power

amplifier can deliver a voltage that is sufficiently high to drive the desired current, while the impedance steadily increases with frequency. In the second regime however, the voltage supplied power amplifier is not sufficient for the increased impedance and the current amplitude drops with  $f^\alpha$ , where alpha is a real constant. To estimate the frequency  $f_{drop}$  at the transition between these two regimes a constant value is assigned to the first part by averaging, and a function  $y(f) = a \cdot f^b$  is fitted to the second regime by linear regression. The intersection of these lines give the characteristic frequencies. For the gradient coils, the frequency is  $f_{gradient} = 14.8\text{kHz}$  and for the offset coils it is  $f_{offset} = 19.6\text{kHz}$ . One can see that just before these frequencies, the current amplitude shortly rises. This is due to the overshoot of the pi-controller. As the power requirements for both PI and power amplifier reach their limits, the PI-controller cannot correctly follow the signal anymore and a distorted version of a sine wave with a certain offset is the resulting current output.

To give a characteristic frequency to which the coils might be driven with the here built power supply,  $f_{offset}$  and  $f_{gradient}$  are sufficient. However, for precise experimental control, it is important to note, that the desired current cannot be supplied correctly in the overshooting regime, just before  $f_{offset}$  and  $f_{gradient}$ . If a bandwidth is to be given at which the plant can respond to a frequency input at all, the 3dB cutoff point might be used. Therefore the 3dB point is drawn as the green horizontal line in Fig. 5.4. The intersection of the fitted lines and the 3dB point is at  $f_{G3dB} = 18.4\text{kHz}$  for the gradient coils and at  $f_{G3dB} = 23.8\text{kHz}$  for the offset coils. Finally, these results are strongly dependent on the desired current amplitude, as higher current amplitudes require higher voltages, thus limiting the frequency response.

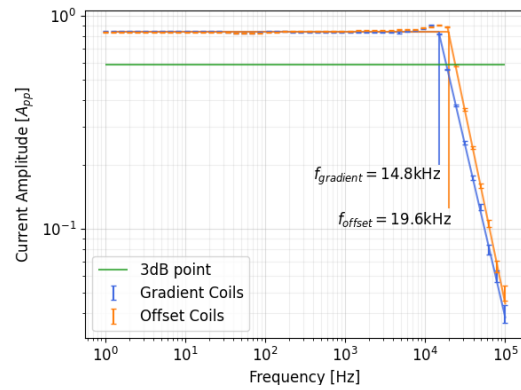


Figure 5.4: Frequency dependence with PI-control

## 5.5 Noise of Power Supply

After precise current control of the here built power supply could be demonstrated and its frequency limits were shown for inductive loads, most importantly the noise level of the supply has to be analysed. After all, this power supply was designed to be a highly precise current source, exhibiting a current noise to amplitude ratio of  $10^{-5}$ . To determine if this

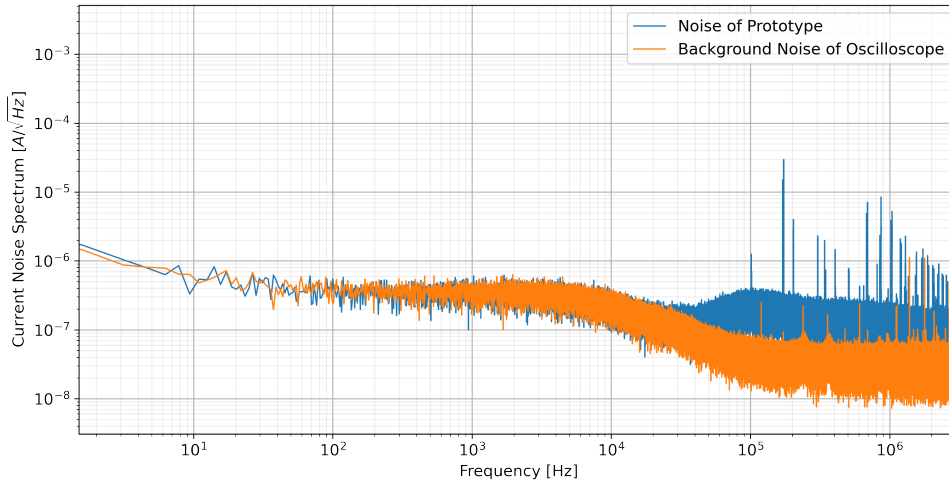


Figure 5.5: Spectral Noise Density

was achieved, a stable set voltage in form of a 1.5V battery is given as an input to the PI controller. The output of the sensing amplifier was recorded with a Handyscope HS6 Diff<sup>4</sup> with a sampling frequency of 6.25MHz, to reduce aliasing in the relevant frequency, and a resolution of 16 bits. To calculate the noise density, a time series of 4 000 000 samples was recorded, the fast Fourier transform (FFT) was performed using python<sup>5</sup> and the power spectrum density (PSD) was calculated according to Sec. 3.2.4. The number of 4M samples was chosen, such that with a 6.25MHz sampling frequency a period of  $\sim 0.6$ s was recorded, which sets the minimal frequency that can be discerned to 1.56Hz. The time series was recorded in AC coupling mode which is specified with a 3dB cutoff frequency of 1.5Hz for the Handyscope. Thus, no lower frequencies can be reasonably measured by the Handyscope.

Five of these PSDs were averaged, to make the white noise level visible more clearly. Then, the linear spectrum density (LSD) could be calculated as explained in Sec. 3.2.4. It is important to note, that the noise level is not artificially decreased by averaging this way. This is, because neither the time series nor the LSDs were averaged, but the power spectral density. By doing so, the average power per frequency (bin) is calculated. This can then be translated into resulting amplitudes, but it is not an average of amplitudes. Averaging amplitudes however reduces noise and cannot be used to analyse the noise level itself. No window function was applied, as is recommended for the measurement of white

<sup>4</sup><https://www.tiepie.com/en/usb-oscilloscope/handyscope-hs6-diff>

<sup>5</sup><https://docs.scipy.org/doc/scipy/tutorial/fft.html>

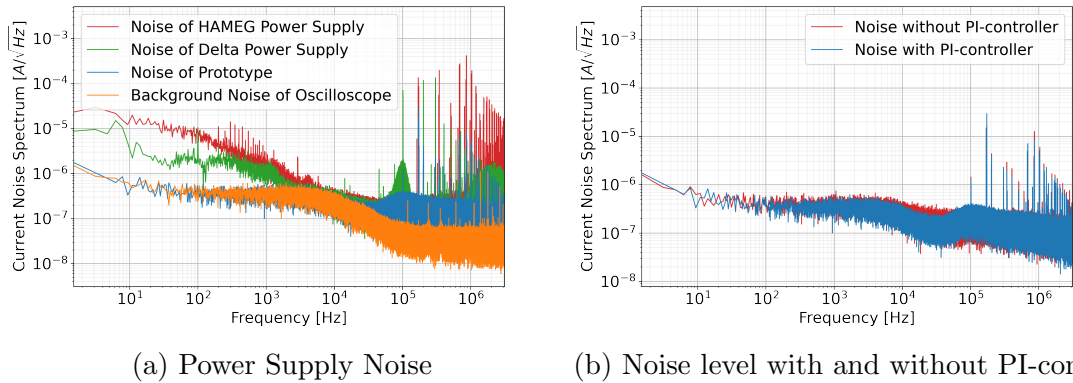


Figure 5.6: Comparison of Different Noise Levels

noise [16].

Fig. 5.5 shows the resulting LSD for a 1.5V set voltage with a coil similar to the coils above connected as a load. In blue, the current noise density is plotted as measured by the sensing amplifier. In orange, the background of noise of the oscilloscope is shown. This was measured with a  $50\Omega$  terminator over the input of the oscilloscope. One can see that for frequencies up to  $\sim 25\text{kHz}$  the current noise density is below the measurement limit of the oscilloscope. As no other, more precise oscilloscope or similar device was at hand, the exact noise level can therefore not be calculated, but an upper bound can be given.

By integrating over the PSD as explained in 3.4 the noise amplitude can be calculated for a given bandwidth. A bandwidth of 23.8kHz was chosen to reflect the 3dB frequency of the offset coils as determined in the chapter above.

The resulting RMS noise calculated according to Eqn. 3.11 is

$$\text{RMS}_{\text{current}} = 2.94 \cdot 10^{-5} \text{A}.$$

The actual RMS noise level of the prototype power supply is therefore somewhere below that level and would need to be determined with a more precise device.

Fig. 5.5 further shows that the noise suppression of the prototype power supply very effective. It eliminates characteristic noise peaks, such as 50Hz line hum, to a point where none are detectable up to 100kHz.

This is further illustrated by Fig. 5.6a. There the noise of the power supplies, powering the prototype, are drawn and compared to the noise of the prototype and the oscilloscope. These measurements were identical to the measurements as explained above. It is clear that the high level of noise, especially in the low frequency regime, does not transfer to

the prototype. Further, the HAMEG supply exhibits a series of high noise peaks between 200Hz and 1kHz, probably stemming from the ripple of the supply. These peaks are not discernible in the noise of the prototype as well, further underlining the effective noise suppression of the device. For frequencies above 100kHz, a significant amount of characteristic noise peaks does show up in the noise density of the prototype, however at these high frequencies the noise will not be translated into the field produced by the coils, as their time response is simply too slow.

Finally, the noise level with and without active PI-controller is compared in Fig. 5.6b. As the Pi-controller contains multiple components, each of these could introduce noise into the system. However, the noise densities are very similar. The noise density with active PI-control shows a certain increase around 100kHz, yet appears to be very slightly lower for lower frequencies. Both exhibit the same characteristic frequency peaks, although for the active PI-controller they are also slightly smaller.

By integration, the RMS noise level over a 23.8kHz bandwidth can again be determined. Without active PI-control the result is

$$\text{RMS}_{noPI} = 3.46 \cdot 10^{-5} \text{A}$$

and is therefore about 18% higher than without PI controller.



## 6 Summary and Outlook

In this thesis, both the design of magnetic coils to create homogeneous offset fields in an ultra-cold dysprosium experiment and a prototype of their ultra-low noise power supply were presented.

It was found, that a small rectangular cage that consists of two interlocking pairs of magnetic coils works best to provide homogeneous offset fields insight a vacuum chamber. At the time of writing this thesis, the coils are being manufactured and can then be tested and included into the new dysprosium experiment under the supervision of Prof. Dr. L. Chomaz.

The prototype of the power supply presents a working prove of concepts and showed promising results so far. The noise level of a DC-current was lower than could be measured in a large part of the relevant bandwidth and its built-in PI-controller could be shown to improve the time response of inductive loads. Before it can be manufactured onto custom printed circuit boards by the electronic workshop of the university and incorporated into the dysprosium experiment however, it will have to be improved upon further. To specify the noise level of the current output of the power supply precisely, instead of just giving an upper limit, a measurement device of higher precision would need to be acquired. Also the PI-controller has to be improved upon, to be able to control high inductive loads, like the designed coils, reliably. Finally, each pair of coils will be supplied by one power supply. All power supplies will then be fitted into a rack to allow for organised experimental control.

The frequency response of the intermediate coils could not be explained to satisfaction, but the current version of the PI-controller presented a definite improvement of the latter. It is up to further investigation, why the frequency dependence of the coil pairs is better than expected from the physical laws of impedance.

In conclusion, this thesis could provide a solid ground to improve upon further. While the rectangular coil cage is ready to be wound, the power supply will still require quite some work and improvement until it can be used in the experiment. But a working prototype was presented and showed promising results. It can therefore be expected, that the final power supply will fulfil the requirements.



## 7 Bibliography

- [1] M. H. Anderson et al. “Observation of Bose-Einstein Condensation in a Dilute Atomic Vapor”. In: *Science* 269.5221 (1995), pp. 198–201. DOI: 10.1126/science.269.5221.198. eprint: <https://www.science.org/doi/pdf/10.1126/science.269.5221.198>. URL: <https://www.science.org/doi/abs/10.1126/science.269.5221.198>.
- [2] T. Maier. “Interactions in a Quantum Gas of Dysprosium Atoms”. Phd Thesis. 5. Physikalisches Institut Universität Stuttgart, Nov. 2015. eprint: <https://www.pi5.uni-stuttgart.de/documents/abgeschlossene-arbeiten/2015-Maier-Thomas-Interactions-in-a-Quantum-Gas-of-Dysprosium-Atoms-PhD.pdf>.
- [3] W. Lunden. “Development of a new Dy quantum gas experiment”. Phd Thesis. Department of Physics at the Massachusetts Institute of Technology, Feb. 2020. eprint: <https://dspace.mit.edu/handle/1721.1/128319>.
- [4] T. Lahaye et al. “The physics of dipolar bosonic quantum gases”. In: *Reports on Progress in Physics* 72.12 (Nov. 2009), p. 126401. DOI: 10.1088/0034-4885/72/12/126401. URL: <https://doi.org/10.1088/0034-4885/72/12/126401>.
- [5] A. J. Moerdijk, B. J. Verhaar, and A. Axelsson. “Resonances in ultracold collisions of  ${}^6\text{Li}$ ,  ${}^7\text{Li}$ , and  ${}^{23}\text{Na}$ ”. In: *Phys. Rev. A* 51 (6 June 1995), pp. 4852–4861. DOI: 10.1103/PhysRevA.51.4852. URL: <https://link.aps.org/doi/10.1103/PhysRevA.51.4852>.
- [6] M. Misakian. “Equations for the Magnetic Field Produced by One or More Rectangular Loops of Wire in the Same Plane”. In: *Journal of Research of the National Institute of Standards and Technology* 105.4 (2000), pp. 557–564. DOI: 10.6028/jres.105.045. eprint: <https://doi.org/10.6028/jres.105.045>.

- [7] Gianmaria Durastante. “Creation of Erbium-Dysprosium Dipolar Quantum Mixtures and Their Interspecies Feshbach Resonances”. PhD thesis. Faculty of Mathematics, Computer Science, and Physics of the University of Innsbruck, Nov. 2020.
- [8] Reza Beiranvand. “Effects of the Winding Cross-Section Shape on the Magnetic Field Uniformity of the High Field Circular Helmholtz Coil Systems”. In: *IEEE Transactions on Industrial Electronics* 64.9 (2017), pp. 7120–7131. DOI: 10.1109/TIE.2017.2686302.
- [9] Arthur H. Firester. “Design of Square Helmholtz Coil Systems”. In: *Review of Scientific Instruments* 37.9 (1966), pp. 1264–1265. DOI: 10.1063/1.1720478. eprint: <https://doi.org/10.1063/1.1720478>.
- [10] Andres Restrepo et al. “A comparative study of the magnetic field homogeneity for circular, square and equilateral triangular Helmholtz coils”. In: (Dec. 2017). DOI: 10.1109/ICEECCOT.2017.8284514.
- [11] William M. Frix, George G. Karady, and Brain A. Venetz. “Comparison of calibration systems for magnetic field measurement equipment”. In: *IEEE Transactions on Power Delivery* 9 (1994), pp. 100–108.
- [12] K. J. Ahrendsen, S. Reyes, and T. J. Gay. “Helmholtz spacing of thin rectangular magnetic field coils”. In: *Review of Scientific Instruments* 91.11 (2020), p. 116103. DOI: 10.1063/5.0023024. eprint: <https://doi.org/10.1063/5.0023024>.
- [13] W. Demtröder. *Experimentalphysik2 Elektrizität und Optik 6. Auflage*. German. Springer Spektrum, 2013. DOI: 10.1007/978-3-642-29944-5.
- [14] G. Heinzl, A. Rüdiger, and R. Schilling. “Spectrum and spectral density estimation by the Discrete Fourier transform (DFT), including a comprehensive list of window functions and some new at-top windows”. In: 2002. eprint: [https://holometer.fnal.gov/GH\\_FFT.pdf](https://holometer.fnal.gov/GH_FFT.pdf).
- [15] James W. Cooley and John W. Tukey. “An Algorithm for the Machine Calculation of Complex Fourier Series”. In: *Mathematics of Computation* 19.90 (1965), pp. 297–301. URL: <http://www.jstor.org/stable/2003354>.
- [16] M. Cerna and A.F. Harvey. *The Fundamentals of FFT-Based Signal Analysis and Measurement*. Application Note 041. National Instruments. July 2000.

- [17] Stefan Scholl. *Exact Signal Measurements using FFT Analysis*. coursematerial. 2016. URL: <http://nbn-resolving.de/urn:nbn:de:hbz:386-kluedo-42930>.
- [18]  $1nV/\sqrt{Hz}$  Low Noise Instrumentation Amplifier. Data Sheet AD8429. Analog Devices. 2017.
- [19] A. Kay. *Operational Amplifier Noise Techniques and Tips for Analyzing and Reducing Noise*. Newnes, Feb. 2012. URL: <https://learning.oreilly.com/library/view/operational-amplifier-noise/9780750685252/>.
- [20] Yu-Meng Yang et al. "Ultra-low noise and high bandwidth bipolar current driver for precise magnetic field control". In: *Review of Scientific Instruments* 90.1 (2019), p. 014701. DOI: 10.1063/1.5046484. eprint: <https://doi.org/10.1063/1.5046484>.
- [21] *High Precision Bulk Metal<sup>®</sup> Foil Surface Mount Current Sensing Chip Resistor with TCR of  $\pm 2$  ppm/ $^{\circ}C$  and Load Life Stability of  $\pm 0.02$  %*. Data Sheet VCS1625. Vishay Precision Group. Feb. 2010.
- [22] *Ultra Precision Resistor (Transfer Molded) MA, MB; MC; MD Series*. Doc.No.: 67002. Alpha Electronics, VPG Brand. Apr. 2016.
- [23] Karl Johan Åström and Tore Hägglund. *PID Controllers: Theory, Design, and Tuning*. English. ISA - The Instrumentation, Systems and Automation Society, 1995.
- [24] *55 V, EMI Enhanced, Zero Drift, Ultralow Noise, Rail-to-Rail Output Operational Amplifiers*. Data Sheet ADA4522-1/ADA4522-2/ADA4522-4. Analog Devices. 2022.
- [25] *High-Voltage, High-Current OPERATIONAL AMPLIFIER*. SBOS093E. Burr-Brown Productions from Texas Instruments. Mar. 1999.
- [26] *Power amplifier stress and power handling limitations*. Application Bulletin AB-039. Burr Brown. 1993.
- [27] J. Lunze. *Regelungstechnik 1*. German. Springer, 2014. DOI: <https://doi.org/10.1007/978-3-642-53909-1>.

- [28] R. Rosok. “Active Magnetic Field Stabilisation for a Quantum Gas Microscope”. Bachelor’s Thesis. 5th Institute of Physics, Universität Stuttgart, Aug. 2021. eprint: <https://www.pi5.uni-stuttgart.de/documents/abgeschlossene-arbeiten/2021-Rosok-Ranga-Active-Magnetic-Field-Stabilisation-for-a-Quantum-Gas-Microscope-BSc.pdf>.

# Acknowledgements

Finally I would like to thank the people who made this thesis possible.

First of all I want to thank Lauriane Chomaz for her excellent and detailed supervision. While providing support at any time, she enabled me to make a meaningful contribution to a new experiment within the context of a bachelor thesis.

Further I want to thank Selim Jochim who agreed to be second examiner.

Also I want to thank Gerhard Zürn, for his very helpful and extensive advice and for providing me with his oscilloscope. I want to thank all members of the Quantum Fluids group and especially Joschka Schöner. Their kind help was always available and working with was a pleasure.

And last but not least, I want to thank my friends and family for always supporting me in every possible way.



# Erklärung

Ich versichere, dass ich diese Arbeit selbstständig verfasst und keine anderen als die angegebenen Quellen und Hilfsmittel verwendet habe.

Heidelberg, den 15.04.2022